

# Thin films dewetting with phase separation: Dependence of surface tension and Hamaker constant on concentration

Javier A. Diez<sup>1</sup>, Alejandro G. González<sup>1</sup>, and Lou Kondic<sup>2</sup>

<sup>1</sup>Instituto de Física Arroyo Seco, Universidad Nacional del Centro de la Provincia de Buenos Aires, CIFICEN-CONICET-CICPBA, Pinto 399, 7000 Tandil, Argentina

<sup>2</sup>Dept. of Mathematical Sciences, Center for Applied Mathematics and Statistics, New Jersey Institute of Technology, Newark, New Jersey 07102, USA

**Abstract** We study the instability of a thin film composed of two miscible fluids (binary fluid) placed on a solid planar surface. We include the fact that both the free surface and wetting energies depend on the mixture concentration. By assuming a linear relationship between these energies and both the bulk and surface concentrations, we analyze their effect on the phase separation of the constituent fluids. The problem is formulated within the gradient dynamics formulation applied to the thin film limit of the Cahn-Hilliard Navier-Stokes equations. The dependence of the free surface energy on concentration leads to a Marangoni type of effect, while the wetting energy resulting from fluid–solid interaction between the film and the substrate is described by a concentration dependent Hamaker constant. The linear stability analysis uncovers that both monotonous and oscillatory evolution is possible. While our problem formulation applies to any binary mixture that can be consistently modeled via the presented approach, a particular interpretation of the results is provided for the case of liquid metal alloy films on nanoscale. In this context, we find that rich dynamics is possible, including the evolution that may lead to formation of drops of the Janus-type as well as of core-shell configurations.

# 1. Introduction

Binary fluids are of much relevance in numerous settings, and have been explored extensively. Modelling problems which include fluid flow combined with phase separation in principle involves resolving a coupled problem of flow, governed by Navier–Stokes formulation, combined with convective and diffusive effects that may be concentration dependent. Extensive research of such problems has been carried out for systems of this type, in particular in the context of oil–recovery and core–annular flows (Joseph & Renardy, 1992*a,b*; Joseph *et al.*, 1997).

In recent decades, there has been significant interest in flow dynamics and stability on much smaller scales, from micro down to nano. In particular, various types of flows and related instabilities have been considered in the context of free surface thin films deposited on solid substrates. Short length scales and flow geometries involve additional complications associated with the presence of free surface, fluid–solid interactions which become in particular relevant on nanoscale, in addition to basic fluid dynamics and phase separation and associated effects. There are, however, also simplifications which could be considered. For many thin film systems, the long wave approximation is appropriate, and additional Cahn–Hilliard formulation (Cahn & Hilliard, 1958) can be used to describe phase separation in a mathematically tractable manner.

While a significant progress has been reached in understanding flow dynamics combined with phase separation, see Oron *et al.* (1997); Craster & Matar (2009) for reviews, there are still many open questions involved in formulating fully self–consistent models describing both film dynamics and phase separation. Significant progress has been reached in the works by Thiele and collaborators (Thiele *et al.*, 2001; Thiele, 2011; Thiele *et al.*, 2013, 2016). These works have formulated the problem in terms of coupled partial differential equations which describe evolving film thickness as well as concentration of two phases (in the case of binary systems), and we will follow similar approach in the present work.

There are numerous binary or ternary systems where phase separation is important, and the formulation that we develop in the present paper is applicable widely (see e.g. Sprenger *et al.* (2003); Clarke (2005); Xu *et al.* (2015); Mao *et al.* (2019); Chao *et al.* (2022)). However, for definiteness and also to be able to connect the results to physical experiments, we focus the discussion in the second part of the paper on liquid metal films on nanoscale. Such films are of particular interest for the application requiring nano-patterning, such as solar cells, plasmonics-related applications, sensing and detection, among others (see Hughes *et al.* (2017); Makarov *et al.* (2016) for reviews). One approach to pattern formation is self- and directed instability involving melting the films by application of laser pulses of duration measured on nanosecond time scale (or even shorter); while melted, films evolve as Newtonian fluids and form drops which solidify into particles once the temperature drops below the melting point. Our focus is on the evolution while the metal is in liquid state; we refer the interested reader to a different problem of solid state dewetting, see recent works focusing on that regime (Khenner, 2018; Khenner & Henner, 2020), as well as a review article (Thompson, 2012).

Liquid state dewetting of films and other geometries is considered widely, and a sig-

nificant progress has been reached in understanding elemental (single fluid) systems, see [Kondic \*et al.\* \(2020\)](#) for a recent review. Some aspects of these systems which are particularly relevant for the present discussion involve the fact that the time scale on which metal films evolve is comparable to the time scales emerging from the stability analysis. The practical consequence of the time scale similarity is that the films may solidify while still evolving. Therefore, in addition to long time asymptotic solutions, often considered when linear stability analysis is performed, transient effects may be important. Analysis of transient behavior constitutes an important part of the analysis carried out in this paper.

In earlier work ([Diez \*et al.\*, 2021](#)), we considered both experimentally and theoretically a bimetallic configuration. That work already produced interesting new results and insights, in particular regarding the competition of film thickness instability and phase separation. A direct comparison to the experimental results considering phase separating Ag–Ni system was found to be favorable in particular regarding the emerging length scales (distance between the formed drops/particles). However, the model used in [Diez \*et al.\* \(2021\)](#) ignored concentration dependence of the fluid–solid interaction forces, and therefore left open a question of whether some features of the experiments could be explained by including such dependence. For example, the experiments ([McKeown \*et al.\*, 2015](#); [Diez \*et al.\*, 2021](#)) find formation of Janus-like as well as of core–shell drops/particles, and one question is whether such structures could be explained theoretically. We will see that the inclusion of concentration dependence of fluid–solid interaction forces leads to a significantly more complex formulation involving a strongly coupled evolution of film thickness and the concentration field. In particular, in contrast to the so-called zeroth case (where dependence of fluid–solid interaction forces is not considered, as in [Thiele \*et al.\* \(2016\)](#); [Diez \*et al.\* \(2021\)](#)), we find oscillatory type of instability development, in addition to the monotonic one. While oscillatory instabilities were found and analyzed in other thin film systems (usually in the context of coupling thermal effects with film evolution ([Shklyaev \*et al.\*, 2012, 2014](#); [Dong & Kondic, 2016](#); [Batson \*et al.\*, 2019](#); [Náráigh & Thiffeault, 2010, 2007](#))), we are not aware of such instabilities being considered in a binary thin film setup.

The paper is organized as follows: In [Sec. 2](#) we present and discuss different contributions to the free energy of the thin film – solid substrate system. In particular, in [Sec. 2.1](#) we discuss gradient dynamics formulation, and in [Sec. 2.2](#) we formulate the problem in nondimensional form. Fluid–solid interaction energy is discussed in [Sec. 2.3](#), and [Sec. 2.4](#) is devoted to the gradient dynamics equations for 3–fields (film thickness, bulk and surface concentrations). Here, we also discuss the limiting expressions for 2–fields (thickness and bulk concentration), which are valid when the width of the surface concentration region is much smaller than the film thickness itself. We also derive the limiting form of the equations for low bulk concentrations. The formulation of the problem in these sections is based to large degree on [Thiele \*et al.\* \(2016\)](#). We proceed by discussing the linear stability analysis (LSA) of the problem when Marangoni and fluid–solid interaction forces depend on bulk and surface concentrations. In [Sec. 3](#), we Fourier transform the equations in space and Laplace transform them in time. This allows us to consider initial conditions in a consistent manner, and it makes the expressions simpler. We

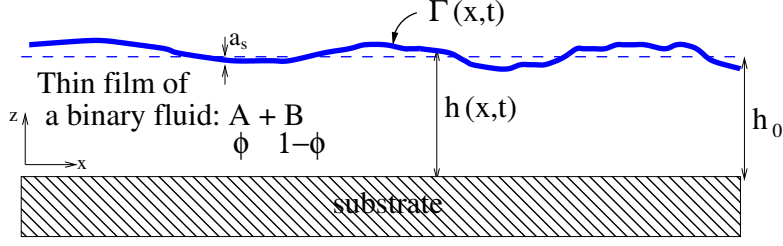


Figure 1: Sketch of the thin film – substrate system showing the main variables of the problem: thickness,  $h$ , volume concentration,  $\phi$  and surface concentration,  $\Gamma$ . Initially, the binary fluid has a volume concentration  $\phi_0$  of fluid  $A$  and  $(1 - \phi_0)$  of fluid  $B$ , as well as a film thickness  $h_0$ .

obtain analytic expressions for the growth rates in a 2–fields description. To interpret in precise terms the results of LSA, we consider in Sec. 4 a particular case of a melted metallic alloy of nanoscale thickness, and discuss how stability properties depend on the parameters of the problem. We conclude by Sec. 5 that summarizes and discusses the main findings of this study.

## 2. Model

We study the instability of a nanometric thin film composed of two miscible fluids (binary fluid) on top of a solid planar surface. Figure 1 illustrates the considered geometry. In the bulk of the film, one of the fluids (say, fluid  $A$ ) has a volumetric concentration,  $c_A(\mathbf{x}, z, t)$ , where  $\mathbf{x} = (x, y)$ , so that its  $z$ –averaged concentration,  $\phi$ , is

$$\phi(\mathbf{x}, t) = \frac{1}{h(\mathbf{x}, t)} \int_0^{h(\mathbf{x}, t)} c_A(\mathbf{x}, z, t) dz = \frac{\psi(\mathbf{x}, t)}{h(\mathbf{x}, t)}.$$

Then, the corresponding  $z$ –averaged concentration of fluid  $B$  is  $1 - \phi$ . Here,  $\psi$ , as defined by the above equation, stands for the amount of fluid  $A$  inside a column of height  $h(\mathbf{x}, t)$  and unit in-plane area. Therefore,  $\psi$  represents an *effective thickness of fluid A*, while  $(h - \psi)$  stands for the effective thickness of fluid  $B$ .

Initially, the thickness of the mixture is  $h_0$ , and the concentration of fluid  $A$  is  $\phi_0$ , so that its effective thickness is  $\psi_0 = \phi_0 h_0$ .

At the free surface of the film, fluid  $A$  is assumed to have a *surface concentration*,  $\Gamma(\mathbf{x}, t)$ . Analogously, the surface concentration of fluid  $B$  is  $1 - \Gamma$ . If  $\Gamma \ll 1$ , then fluid  $A$  acts as a soluble surfactant with surface concentration  $\Gamma$  and volume concentration  $\phi$ . Conversely, if  $1 - \Gamma \ll 1$ , then fluid  $B$  can be considered as a surfactant. We also allow for an exchange of fluids  $A$  and  $B$  between the surface and the bulk. We do not consider mass exchange with the gaseous phase above the binary film. Note that conservation of mass at the free surface implies  $\Gamma dS_f = \tilde{\Gamma} dS$ , where  $dS_f$  is the element of the free surface,  $h(\mathbf{x}, t)$ , and  $\tilde{\Gamma}$  is the projected concentration on the plane element  $dS = dx dy$ . Thus, we have  $\tilde{\Gamma} = \Gamma \xi$ ,  $\xi = \sqrt{1 + |\nabla h|^2}$ .

## 2.1. Gradient dynamics formulation

Here, we provide a brief overview of the formulation developed in [Thiele \*et al.\* \(2016\)](#), where the gradient dynamics approach is extended to describe the non-equilibrium dissipative dynamics of thin-film systems with several variables and to cast the dynamic equations into a form that reproduces Onsager's reciprocity relations.

We start by considering the corresponding free energy functional

$$\mathcal{F} = \int \left[ F_{fs}(h, \Gamma, \phi) + h g(\phi) + \frac{\sigma}{2} h |\nabla(\phi)|^2 + \frac{\sigma_s}{2\xi} |\nabla(\Gamma)|^2 + \xi f_s(\Gamma) \right] dS. \quad (1)$$

The first term in Eq. (1) corresponds to the energy per unit surface of the inter-atomic/molecular interaction between the fluid in the film and the solid substrate. We write it in general form as

$$F_{fs} = \hat{K} \gamma_{ref} F_{fs}(h, \Gamma, \phi),$$

where, for later convenience, we define the nondimensional constant

$$\hat{K} = \frac{\mathcal{H}_{ref}}{6\pi\gamma_{ref}h_c^2}, \quad (2)$$

and  $\gamma_{ref}$ ,  $\mathcal{H}_{ref}$  are reference values of surface tension and Hamaker constant, respectively. We consider a dependence on both  $\Gamma$  and  $\phi$  since atoms/molecules in the bulk as well as at the free surface take part in the interaction with atoms/molecules in the substrate.

The function  $g(\phi)$  in the second term of Eq. (1) represents the bulk Gibbs energy per unit volume. For convenience, we write it as

$$g(\phi) = \mathcal{E}G(\phi), \quad \mathcal{E} = \frac{k_B T}{a^3},$$

where  $G$  is a nondimensional function and  $a$  is an atomic/molecular length scale in the fluid bulk (e.g., the radius of a spherical atom/molecule ([Thiele, 2011](#))).

The third and fourth terms in Eq. (1) stand for the energetic contribution of strong gradients in both bulk,  $\phi$ , and surface,  $\Gamma$ , concentrations, where  $\sigma$  (energy per unit length) and  $\sigma_s$  (energy) denote the interfacial stiffness of the diffuse interface between the pure fluids in the bulk and at the free surface, respectively. These parameters are estimated by assuming that the effective thicknesses of the diffuse interfaces are of the order of  $a$  and  $a_s$ , respectively. Also, we consider that  $\sigma$  and  $\sigma_s$  are related to the interfacial tension between  $A$  and  $B$  fluids,  $\gamma_{AB}$ , as  $\sigma = a\gamma_{AB}$ ,  $\sigma_s = a_s^2\gamma_{AB}$ . The value of  $\gamma_{AB}$  can be estimated by means of the Girifalco–Good formula,

$$\gamma_{AB} = \gamma_A + \gamma_B - 2C_G (\gamma_A\gamma_B)^{1/2},$$

where  $C_G$  is a constant close to unity for most of the fluids ([Girifalco & Good, 1957](#)).

The last term in Eq. (1) stands for the free energy contribution due to the presence of molecules of both fluids at the interface. We write it as  $f_s(\Gamma) = \gamma_{ref}F_s(\Gamma)$ . According

to the formulation in [Thiele \*et al.\* \(2016\)](#) (e.g., in their Eq. (B27)), this function defines the general expression of surface tension as

$$\gamma(h, \Gamma, \phi) = f_s - \Gamma \frac{\partial f_s}{\partial \Gamma} - \Gamma \frac{\partial F_{fs}}{\partial \Gamma} - \frac{\sigma_s}{2} (\nabla \Gamma)^2 + \sigma_s \Gamma \nabla^2 \Gamma. \quad (3)$$

The dependence of  $\gamma$  on the surface concentration,  $\Gamma$ , is not surprising. However, the fluid-solid interaction energy (third term on the r.h.s. of Eq. (3)) introduces new dependencies on both  $\phi$  and  $h$ . This is because the long-range forces include interactions between molecules in the bulk, whose amount depend on both  $\phi$  and  $h$ , and those in the substrate. Here, we will consider the nondimensional surface energy as ([Thiele \*et al.\*, 2016](#)),

$$F_s(\Gamma) = 1 + \nu \Gamma (\log \Gamma - 1).$$

Then, the surface tension of the binary fluid is given by

$$\gamma(h, \Gamma, \phi) = \gamma_{ref} \left[ 1 - \Gamma \left( \nu + \hat{K} \frac{\partial F_{fs}}{\partial \Gamma} \right) \right] - \sigma_s \left[ \frac{1}{2} (\nabla \Gamma)^2 - \Gamma \nabla^2 \Gamma \right]. \quad (4)$$

Note that the dependence of  $\gamma$  on  $h$  and  $\phi$  is direct consequence of a non-zero  $\partial F_{fs}/\partial \Gamma$ .

## 2.2. Nondimensional formulation

From now on, we consider a *nondimensional* formulation by expressing the thicknesses  $h$  and  $\psi$  in units of the initially ( $t = 0$ ) flat thickness of the film,  $h_0$ . The in-plane coordinates  $(x, y)$  are expressed in units of an arbitrary length  $\ell$ , and  $t$  is in units of the characteristic time

$$t_c = \frac{3\eta\ell^4}{\gamma_{ref}h_0^3}, \quad (5)$$

where  $\eta$  is the viscosity of the film. Therefore, the *nondimensional* free energy in Eq. (1), in units of  $\gamma_{ref}h_0^2$ , takes the form

$$\mathcal{F} = \int \mathcal{F}_s dS = \int \left[ K F_{fs}(h, \Gamma, \phi) + \beta h G(\phi) + \frac{\Sigma}{2} h |\nabla \phi|^2 + \frac{\Sigma_s}{2\xi} |\nabla \Gamma|^2 + \xi F_s(\Gamma) \right] dS, \quad (6)$$

where the parameters are defined as

$$\Sigma = \frac{\sigma}{\gamma_{ref}h_0}, \quad \Sigma_s = \frac{\sigma_s}{\gamma_0 h_0^2}, \quad K = \frac{\hat{K}}{\delta^2} = \frac{\mathcal{H}_{ref}\ell^2}{6\pi\gamma_{ref}h_e^2 h_0^2}, \quad \beta = \frac{k_B T \ell^2}{\gamma_{ref} a^3 h_0}, \quad \delta = \frac{h_0}{\ell}.$$

Table 1 gives a summary of the dimensional parameters and their combinations that has been used for the nondimensionalization of the equations that follow.

In the following, we consider the general formulation of the gradient dynamics for a given expression of the total free energy,  $\mathcal{F}$ . Thus, we write the coupled evolution equations (Eqs. (42) to (45) developed in [Thiele \*et al.\* \(2016\)](#)) for the three fields in

the framework of linear non-equilibrium thermodynamics and long wave approximation ( $\delta \ll 1$ ) as

$$\frac{\partial h}{\partial t} + \nabla \cdot \left[ -h^3 \nabla \frac{\delta \mathcal{F}}{\delta h} - \frac{3}{2} h^2 \Gamma \nabla \frac{\delta \mathcal{F}}{\delta \Gamma} - h^2 \psi \nabla \frac{\delta \mathcal{F}}{\delta \psi} \right] = 0, \quad (7a)$$

$$\frac{\partial \Gamma}{\partial t} + \nabla \cdot \left[ -\frac{3}{2} h^2 \Gamma \nabla \frac{\delta \mathcal{F}}{\delta h} - (3h\Gamma^2 + 3D_s \Gamma) \nabla \frac{\delta \mathcal{F}}{\delta \Gamma} - \frac{3}{2} h \psi \Gamma \nabla \frac{\delta \mathcal{F}}{\delta \psi} \right] = -\tilde{J}_{ad}, \quad (7b)$$

$$\frac{\partial \psi}{\partial t} + \nabla \cdot \left[ -h^2 \psi \nabla \frac{\delta \mathcal{F}}{\delta h} - \frac{3}{2} h \psi \Gamma \nabla \frac{\delta \mathcal{F}}{\delta \Gamma} - (h\psi^2 + 3D\psi) \nabla \frac{\delta \mathcal{F}}{\delta \psi} \right] = J_{ad}. \quad (7c)$$

Here, we have defined the nondimensional parameters

$$D = \frac{M}{h_0^2} = \frac{\mathcal{D}\eta}{\mathcal{E}h_0^2} = \frac{\mathcal{D}\eta a^3}{k_B T h_0^2}, \quad D_s = \frac{M_s}{h_0} = \frac{\mathcal{D}_s \eta}{\mathcal{E}_s h_0} = \frac{\mathcal{D}_s \eta a_s^2}{k_B T h_0},$$

where  $M$  and  $M_s$  are the molecular mobilities in the bulk and the surface, respectively, which are related to the molecular energy densities  $\mathcal{E}$  and  $\mathcal{E}_s$  through the molecular diffusion coefficients of the binary fluid for the bulk and surface,  $\mathcal{D}$  and  $\mathcal{D}_s$ , respectively. Note that the definition of  $\mathcal{D}$  agrees with Stokes-Einstein's relation if  $M = a^2/6\pi$ . We note that the value of  $\mathcal{D}$  is not enough to determine  $M$ , since one still needs to estimate  $a$ . This quantity is of the order of the nanometer and it is related to diffusion processes in the bulk. One also needs the value of  $a_s$ , which is associated with adsorption and desorption processes in the surface, so that it is expected to be even smaller than  $a$  (Diamant & Andelman, 1996). It is usual to consider  $a \approx a_s$ , and we use this approximation here; also we assume that  $\mathcal{D}_s \approx \mathcal{D}$ .

The right hand side of Eqs. (7b) and (7c) corresponds to the adsorption-desorption flux between the bulk and the surface. It is given by

$$\tilde{J}_{ad} = 3D_s \Gamma^2 \left( \frac{1}{s} \frac{\delta \mathcal{F}}{\delta \Gamma} - \frac{\delta \mathcal{F}}{\delta \psi} \right) = \frac{J_{ad}}{s},$$

where  $s = a_s/h_0$ .

Based on the energy functional specified by Eq. (6), and under the long-wave approximation we have (see the Appendix in Thiele *et al.* (2016))

$$p \equiv \frac{\delta \mathcal{F}}{\delta h} = -\nabla [\hat{\gamma}(\Gamma, h) \nabla h] + K \frac{\partial F_{fs}}{\partial h} - K \frac{\psi}{h^2} \frac{\partial F_{fs}}{\partial \phi} + \beta \left( G - \frac{\psi}{h} \frac{\partial G}{\partial \phi} \right) + \Sigma \left( -\frac{2\psi}{h^3} \nabla h \cdot \nabla \psi + \frac{(\nabla \psi)^2}{2h^2} + \frac{3\psi^2}{2h^4} (\nabla h)^2 - \frac{\psi^2}{h^3} \nabla^2 h + \frac{\psi}{h^2} \nabla^2 \psi \right) \quad (8)$$

$$\mu_s \equiv \frac{\delta \mathcal{F}}{\delta \Gamma} = \frac{1}{\delta^2} \frac{\partial F_s}{\partial \Gamma} + K \frac{\partial F_{fs}}{\partial \Gamma} - \Sigma_s \nabla^2 \Gamma, \quad (9)$$

$$\mu \equiv \frac{\delta \mathcal{F}}{\delta \psi} = \frac{K}{h} \frac{\partial F_{fs}}{\partial \phi} + \beta \frac{\partial G}{\partial \phi} + \Sigma \left( -\frac{\psi}{h^3} (\nabla h)^2 + \frac{\nabla h \cdot \nabla \psi}{h^2} + \frac{\psi}{h^2} \nabla^2 h - \frac{\nabla^2 \psi}{h} \right), \quad (10)$$

where

$$\hat{\gamma}(\Gamma, h) = \frac{\gamma}{\gamma_{ref}} = F_s - \Gamma \frac{\partial F_s}{\partial \Gamma} - \Gamma \hat{K} \frac{\partial F_{fs}}{\partial \Gamma} - \frac{\hat{\Sigma}_s}{2} (\nabla \Gamma)^2 + \hat{\Sigma}_s \Gamma \nabla^2 \Gamma, \quad (11)$$

is the nondimensional version of Eq. (3) (here  $\hat{\Sigma}_s = \Sigma_s \delta^2$ ). In Eqs. (8)–(10),  $p$  stands for pressure, and  $\mu_s, \mu$  stand for surface and bulk chemical potentials, respectively. Here,  $p$  and  $\mu$  are given in units of  $\gamma_{ref} h_0 / \ell^2$  and  $\mu_s$  in units of  $\gamma_{ref} \delta^2$ .

Let us now consider the physical interpretation of the terms in Eqs. (8)–(10). The total pressure,  $p$ , can be written as

$$p = p_{cap} + p_{fs} + p_{osm} + p_{diff}, \quad (12)$$

where

$$\begin{aligned} p_{cap} &= -\nabla [\hat{\gamma}(\Gamma, h) \nabla h], \quad p_{fs} = K \left( \frac{\partial F_{fs}}{\partial h} - \frac{\psi}{h^2} \frac{\partial F_{fs}}{\partial \phi} \right), \quad p_{osm} = \beta \left( G - \frac{\psi}{h} \frac{\partial G}{\partial \phi} \right), \\ p_{diff} &= \Sigma \left( -\frac{2\psi}{h^3} \nabla h \cdot \nabla \psi + \frac{1}{2h^2} (\nabla \psi)^2 + \frac{3\psi^2}{2h^4} (\nabla h)^2 - \frac{\psi^2}{h^3} \nabla^2 h + \frac{\psi}{h^2} \nabla^2 \psi \right). \end{aligned} \quad (13)$$

The last pressure component, related to diffuse interfaces, can also be found in the literature (see e.g. Thiele *et al.* (2013); Doi (2011)) in terms of  $\phi$  as

$$p_{diff} = \Sigma \left( \frac{1}{2} (\nabla \phi)^2 + \frac{\phi}{h} \nabla h \cdot \nabla \phi + \phi \nabla^2 \phi \right). \quad (14)$$

The surface chemical potential,  $\mu_s$ , in Eq. (9) includes the contributions due to the Marangoni effects, i.e., the dependence of surface tension,  $\gamma$ , on surface concentration,  $\Gamma$  (see Eq. (11)). These contributions can be separated as

$$\mu_s = \mu_{s,osm} + \mu_{s,rig}, \quad (15)$$

where

$$\mu_{s,osm} = \frac{1}{\delta^2} \frac{\partial F_s}{\partial \Gamma} + K \frac{\partial F_{fs}}{\partial \Gamma}, \quad \mu_{s,rig} = -\Sigma_s \nabla^2 \Gamma. \quad (16)$$

Thus, the first one (osmotic contribution) accounts for the variation of the surface energy with respect to the surface concentration while the second one for the effect of the surface rigidity.

Finally, the bulk chemical potential,  $\mu$ , in Eq. (10) has three contributions:

$$\mu = \mu_{fs} + \mu_{osm} + \mu_{diff}, \quad (17)$$

where

$$\begin{aligned} \mu_{fs} &= \frac{K}{h} \frac{\partial F_{fs}}{\partial \phi}, \quad \mu_{osm} = \beta \frac{\partial G}{\partial \phi}, \\ \mu_{diff} &= -\frac{\Sigma}{h} \left( \frac{\psi}{h^2} (\nabla h)^2 - \frac{1}{h} \nabla h \cdot \nabla \psi - \frac{\psi}{h} \nabla^2 h + \nabla^2 \psi \right) = -\frac{\Sigma}{h} \nabla \cdot (h \nabla \phi). \end{aligned} \quad (18)$$

We note that all three contributions to  $\mu$  depend on  $h$  and the bulk concentration,  $\phi$ , and not explicitly on  $\Gamma$ .



<i>Variable</i>	<i>Symbol</i>	<i>In units of</i>
in-plane coordinates	$x, y$	$\ell$
thickness, aver. bulk concentration	$h, \psi$	$h_0$
time	$t$	$3\eta_0\ell^4/(\gamma_{ref}h_0^3)$
surface tension	$\hat{\gamma}$	$\gamma_{ref}$
surface and bulk concentrations	$\Gamma, \phi$	1
free energy	$\mathcal{F}$	$\gamma_{ref}h_0^2$
pressure, bulk chemical potential	$p, \mu$	$\gamma_{ref}h_0/\ell^2$
surface chemical potential	$\mu_s$	$\gamma_{ref}h_0^2/\ell^2$

Table 1: Scales of the nondimensional variables used in the the equations.

Note that Eq. (7a) is in conservative form, in agreement with the fact that the film thickness  $h(\mathbf{x}, t)$  is a *conserved field*, i.e.,

$$\int h(\mathbf{x}, t) dS = V = V_A + V_B = const,$$

where  $V$  is the volume of the binary fluid and  $V_A, V_B$  are the volumes of the pure fluids, respectively. On the other hand, note also that both Eqs. (7b) and (7c) have non zero right hand sides, which account for the mass transfer between the surface and the bulk. Therefore, neither  $\int \Gamma(\mathbf{x}, t) dS$  nor  $\int \psi(\mathbf{x}, t) dS$  are conserved. However, if we multiply Eq. (7b) by  $s$  and add it to Eq. (7c), we obtain

$$\frac{\partial \tilde{\psi}}{\partial t} + \nabla \cdot \left[ -h^2 \left( \tilde{\psi} + s \frac{\Gamma}{2} \right) \nabla p - 3\Gamma \left( \frac{h\tilde{\psi}}{2} + s \frac{h\Gamma}{2} + s D_s \right) \nabla \mu_s - \psi \left( h\tilde{\psi} + s \frac{h\Gamma}{2} + 3D \right) \nabla \mu \right] = 0, \quad (20)$$

which is in conservative form for  $\tilde{\psi} = \psi + s\Gamma$ . Then,

$$\int \tilde{\psi} dS = \int (\psi + s\Gamma) dS = \int \phi dV + \int s\Gamma dS = V_A^{bulk} + V_A^{surf} = V_A = const.,$$

which also implies the conservation of  $V_B$ .

### 2.3. Model for fluid-solid interaction energy

In order to explore the influence of  $\Gamma$  and  $\phi$  on the film evolution, we propose a very simple functional form where the fluid-solid energy depends only on a linear combination of both concentrations, instead of depending on them separately. Thus, we assume that  $F_{fs}$  can be written as

$$F_{fs}(h, \Gamma, \phi) = F_{fs}(h, \Phi), \quad \Phi = \chi\Gamma + (1 - \chi)\phi, \quad 0 \leq \chi \leq 1, \quad (21)$$

where  $\chi$  is the control parameter, specifying the degree to which fluid-solid interaction forces depend on  $\phi$  and  $\Gamma$ . Therefore, in the fluid-solid interaction terms of the expressions given so far, we express the derivatives in terms of new set of variables  $(\chi, \Phi)$  as

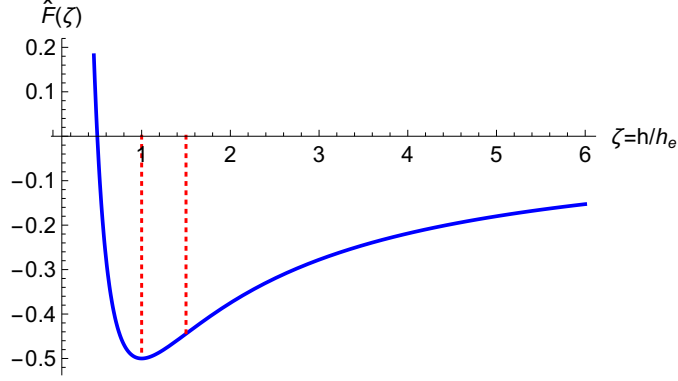


Figure 2: Fluid-solid interaction energy,  $\hat{F}(\zeta)$ , as a function of  $\zeta = h/h_e$  for  $n = 3$  and  $m = 2$ . The vertical dotted red lines indicate the points where  $\hat{F}' = 0$  ( $\zeta = 1$ ) and  $\hat{F}'' = 0$  ( $\zeta = e^{\ln(m/n)/(m-n)} = 1.5$ ).

follows

$$\frac{\partial F_{fs}}{\partial \Gamma} = \chi \frac{\partial F_{fs}}{\partial \Phi}, \quad \frac{\partial F_{fs}}{\partial \phi} = (1 - \chi) \frac{\partial F_{fs}}{\partial \Phi}.$$

Moreover, we consider a simplified version of the dependence of fluid-solid energy,  $F_{fs}(h, \Phi)$  in Eq. (21), assuming that the dependence on  $h$  and  $\Phi$  are separable

$$F_{fs}(h, \Phi) = \frac{\mathcal{H}(\Phi)}{\mathcal{H}_{ref}} \hat{F}(h). \quad (22)$$

Here, there is a single effective Hamaker constant,  $\mathcal{H}(\Phi)$ , for both attractive and repulsive forces, which is assumed to depend on  $\Phi$ . We further assume that  $\mathcal{H}(\Phi)$  depends linearly on  $\Phi$  as

$$\mathcal{H}(\Phi) = \Phi \mathcal{H}_A + (1 - \Phi) \mathcal{H}_B = \mathcal{H}_B (1 + \tau \Phi) \quad (23)$$

where

$$\tau = \frac{\mathcal{H}_A}{\mathcal{H}_B} - 1. \quad (24)$$

Since both  $\mathcal{H}_A$  and  $\mathcal{H}_B$  are positive, we have  $\tau > -1$ . In order to simplify Eq. (22), we choose  $\mathcal{H}_{ref} = \mathcal{H}_B$ .

Regarding the  $h$ -dependence, we consider a power-law dependence of  $\hat{F}$  on  $h$ , as (see Israelachvili (1992))

$$\hat{F}(h) = \frac{\zeta^{1-n}}{n-1} - \frac{\zeta^{1-m}}{m-1}, \quad \zeta = \frac{h}{h_e},$$

for  $n > m$  (typically  $(n, m) = (3, 2)$ ) (see Fig. 2).

Thus, the potential  $F_{fs}$  is determined by the constant  $h_e$  and the coefficient  $\tau$  in the dependence of  $\mathcal{H}$  on  $\Phi$  as in Eq. (23).

We note that using the presented form of fluid-solid interaction energy, Eq. (11), yields the surface tension of the mixture as

$$\hat{\gamma}(h, \phi, \Gamma) = 1 - \nu(\tau) \Gamma - \tau \chi \hat{K} \Gamma \hat{F}(h) - \frac{\hat{\Sigma}_s}{2} (\nabla \Gamma)^2 + \hat{\Sigma}_s \Gamma \nabla^2 \Gamma. \quad (25)$$

Here,  $\nu(\tau)$  is determined by the condition that for a film of thickness  $h_0$  with *uniform* bulk and surface concentrations ( $\phi = \Gamma = 1$ ), the surface tension is that of liquid  $A$ ,  $\gamma_A$ . Thus, we have

$$\nu(\tau) = \nu_0 - \tau\chi\hat{K}\hat{F}(h_0), \quad (26)$$

where

$$\nu_0 = 1 - \frac{\gamma_A}{\gamma_B} \quad (27)$$

is the value of  $\nu$  for  $\chi = 0$  or  $\tau = 0$ . In the following, we will assume that fluids  $A$  and  $B$  are chosen such that  $\nu_0 > 0$  ( $\gamma_A < \gamma_B$ ), leading to usual Marangoni effect, and we will take  $\gamma_{ref} = \gamma_B$ .

## 2.4. Reduction to two fields

Here we proceed with the reduction from three to two fields, which is appropriate in the case of very fast adsorption and desorption, that is, transfer between volume and surface concentration. For details of reduction procedure we refer the reader to [Thiele \*et al.\* \(2016\)](#); we only note that mathematically this limits can be obtained in the limit  $s \ll 1$ , with the final outcome that  $\tilde{\psi} \rightarrow \psi$  and  $\Gamma \rightarrow \phi$ . We also refer to the reader to [Thiele \*et al.\* \(2016\)](#) for the discussion regarding the connection between this reduction and gradient dynamics framework.

Thus, Eqs. (7a) and (20) form the two field formulation for  $(h, \psi)$ ,

$$\frac{\partial h}{\partial t} + \nabla \cdot \left[ -h^3 \nabla p - \frac{3}{2} h \psi \nabla \mu_s - h^2 \psi \nabla \mu \right] = 0, \quad (28a)$$

$$\frac{\partial \psi}{\partial t} + \nabla \cdot \left[ -h^2 \psi \nabla p - \frac{3}{2} \psi^2 \nabla \mu_s - (h \psi^2 + 3D\psi) \nabla \mu \right] = 0, \quad (28b)$$

where  $p$ ,  $\mu$  and  $\mu_s$  are given by (see Eqs. (12) and (17)),

$$\begin{aligned} p = & -\nabla [\hat{\gamma}(\phi, h) \nabla h] + K \frac{\partial F_{fs}}{\partial h} - K(1 - \chi) \frac{\psi}{h^2} \frac{\partial F_{fs}}{\partial \Phi} + \beta \left( G - \frac{\psi}{h} \frac{\partial G}{\partial \phi} \right) + \\ & + \Sigma \left( -\frac{2\psi}{h^3} \nabla h \cdot \nabla \psi + \frac{1}{2h^2} (\nabla \psi)^2 + \frac{3\psi^2}{2h^4} (\nabla h)^2 - \frac{\psi^2}{h^3} \nabla^2 h + \frac{\psi}{h^2} \nabla^2 \psi \right), \end{aligned} \quad (29)$$

$$\begin{aligned} \mu = & (1 - \chi) \frac{K}{h} \frac{\partial F_{fs}}{\partial \Phi} + \beta \frac{\partial G}{\partial \phi} + \\ & + \Sigma \left( -\frac{\psi}{h^3} (\nabla h)^2 + \frac{1}{h^2} \nabla h \cdot \nabla \psi + \frac{\psi}{h^2} \nabla^2 h - \frac{1}{h} \nabla^2 \psi \right), \end{aligned} \quad (30)$$

and (see Eqs. (11) and (15))

$$\mu_s = \frac{1}{\delta^2} \frac{\partial F_s}{\partial \phi} + \chi K \frac{\partial F_{fs}}{\partial \Phi} \quad (31)$$

$$\hat{\gamma}(\phi, h) = \frac{\gamma}{\gamma_{ref}} = F_s - \phi \frac{\partial F_s}{\partial \phi} - \chi \phi \hat{K} \frac{\partial F_{fs}}{\partial \Phi}, \quad (32)$$

since now we have  $\Sigma_s = 0$  and  $\Gamma = \phi$ . We note that the presented formulation is appropriate for numerical simulations due to being written in conservation form.

In order to compare these expressions with other ones in the literature (Thiele *et al.*, 2013; Todorova, 2013), we write them in terms of  $(h, \phi)$  as

$$\frac{\partial h}{\partial t} + \nabla \cdot \left[ -h^3 \nabla p - \frac{3}{2} h^2 \phi \nabla \mu_s - h^3 \phi \nabla \mu \right] = 0, \quad (33a)$$

$$\frac{\partial(h\phi)}{\partial t} + \nabla \cdot \left[ -h^3 \phi \nabla p - \frac{3}{2} h^2 \phi^2 \nabla \mu_s - (h^3 \phi^2 + 3Dh\phi) \nabla \mu \right] = 0, \quad (33b)$$

where  $p$  and  $\mu$  are given as

$$p = -\nabla [\hat{\gamma}(\phi, h) \nabla h] + K \frac{\partial F_{fs}}{\partial h} - (1 - \chi) K \frac{\phi}{h} \frac{\partial F_{fs}}{\partial \Phi} + \beta \left( G - \frac{\psi}{h} \frac{\partial G}{\partial \phi} \right) + \Sigma \left( \frac{1}{2} (\nabla \phi)^2 + \frac{\phi}{h} \nabla h \cdot \nabla \phi + \phi \nabla^2 \phi \right), \quad (34)$$

$$\mu = (1 - \chi) \frac{K}{h} \frac{\partial F_{fs}}{\partial \Phi} + \beta \frac{\partial G}{\partial \phi} - \frac{\Sigma}{h} \nabla \cdot (h \nabla \phi). \quad (35)$$

In the Appendix A we show that in the limit of low concentrations this formulation reduces to the usual expressions found in the literature when the rigidities vanish ( $\Sigma = \Sigma_s = 0$ ), only the low-concentration entropic (ideal gas) terms in the energies are considered, and nonlinear interaction terms are neglected (Karpitschka & Riegler, 2012, 2014; Thiele *et al.*, 2016).

### 3. Linear stability analysis (LSA)

We proceed by discussing the LSA, which allows to extract important physical insights from a highly complicated nonlinear problem. A basic understanding can be reached by considering an initially flat thin film, i. e.,  $h_0 = 1$  and  $\psi_0 = \phi_0 < 1$  at  $t = 0$ . We will consider here only the 2-fields formulation in two spatial dimensions. Before proceeding, we note that (simple) zero-case, corresponding to the simplification where neither differences in surface tensions nor concentration dependence are considered ( $\tau = \nu_0 = 0$ ) was considered in our earlier work (Diez *et al.*, 2021).

We analyze the behavior of Eqs. (28a) and (28b) under perturbations of the initial state

$$h(x, t) = 1 + \epsilon h_p(x, t), \quad \psi(x, t) = \phi_0 + \epsilon \psi_p(x, t)$$

where  $\epsilon \ll 1$ . First, we express the perturbations by using their Fourier transforms

$$h_p(x, t) = \int_{-\infty}^{\infty} \hat{h}(k, t) e^{ikx} dk, \quad \psi_p(x, t) = \int_{-\infty}^{\infty} \hat{\psi}(k, t) e^{ikx} dk, \quad (36)$$

where  $k$  is a wavenumber. After linearizing Eqs. (28a) and (28b) to order  $\epsilon$  and using Eq. (36), we obtain a linear system of equations for  $\hat{h}$  and  $\hat{\psi}$ :

$$\begin{pmatrix} \frac{d}{dt} - \omega_h & a_h \\ a_\psi & \frac{d}{dt} - \omega_\psi \end{pmatrix} \begin{pmatrix} \hat{h}(k, t) \\ \hat{\psi}(k, t) \end{pmatrix} = 0, \quad (37)$$

where

$$\begin{aligned} a_h &= B_1 k^2, & \omega_h &= \omega_h^0 + \phi_0 a_h + \phi_0 k^2 (B_2 + \nu_0 k^2), \\ \omega_\psi &= \omega_\psi^0 - \phi_0 a_h, & a_\psi &= \phi_0 (\omega_\psi - \omega_h + \phi_0 a_h + B_3 k^2), \end{aligned} \quad (38)$$

and the reference frequencies for  $\nu_0 = \tau = 0$  (zero case) are

$$\omega_h^0 = k^2 (\hat{k}_h^2 - k^2), \quad (39)$$

$$\omega_\psi^0 = \hat{\omega}_\psi^0 k^2 (\hat{k}_\psi^2 - k^2), \quad (40)$$

where

$$\hat{k}_h^2 = -K \hat{F}_0'', \quad \hat{k}_\psi^2 = -\frac{\beta G_0''}{\Sigma}, \quad \hat{\omega}_\psi^0 = 3D\Sigma\phi_0. \quad (41)$$

The coefficients  $B_i$ ,  $i = 1, 2, 3$  are given by

$$\begin{aligned} B_1 &= \frac{3\nu_0}{2\delta^2} + \tau K \left[ \hat{F}_0' - \left(1 + \frac{\chi}{2}\right) \hat{F}_0 \right], & B_2 &= -\tau K \left( \frac{3}{2} \chi \hat{F}_0' + \hat{F}_0'' \right), \\ B_3 &= 3\tau K D (1 - \chi) (\hat{F}_0' - \hat{F}_0). \end{aligned} \quad (42)$$

Here, the 0 superscript in  $\hat{F}$  and  $G$  stands for the evaluation at  $h = 1$  and  $\phi = \phi_0$ , and the primes stand for derivatives. Note that for  $\tau = 0$ , i. e., without concentration effects in fluid-solid interaction forces, we have  $B_2 = B_3 = 0$ , but  $B_1$  is nonzero, showing that stability properties of the film are influenced by concentration dependence of surface tension, as expected. For  $\tau \neq 0$ , we note that while  $\hat{F}^0 < 0$  always,  $\hat{F}_0'$  and  $\hat{F}_0''$  could in principle change sign. However, since for  $\zeta > 2$  (which is the interval of interest) both of these quantities are positive, and therefore the signs of  $B_2$  and  $B_3$  are determined by  $\tau$  as  $\text{sgn}(B_2) = -\text{sgn}(\tau)$  and  $\text{sgn}(B_3) = \text{sgn}(\tau)$ . On the other hand,  $B_1$  could be of either sign.

Since we are interested not only in the long time evolution but also in the transient behaviour of the instability, as discussed further in the context of metal films in Sec. 4, we solve the temporal problem by using the Laplace transform method. In the present context, the use of Laplace transform also simplifies significantly the interpretation of the results. The outcome of Fourier analysis (in time) is briefly discussed in Sec. 3.6.

Applying Laplace transform to Eq. (37), we obtain

$$\mathbb{M} \begin{pmatrix} H(k, \omega) \\ \Psi(k, \omega) \end{pmatrix} = \begin{pmatrix} \omega - \omega_h & a_h \\ a_\psi & \omega - \omega_\psi \end{pmatrix} \begin{pmatrix} H(k, \omega) \\ \Psi(k, \omega) \end{pmatrix} = \begin{pmatrix} \hat{h}(k, 0) \\ \hat{\psi}(k, 0) \end{pmatrix} \quad (43)$$

where  $H(k, \omega)$  and  $\Psi(k, \omega)$  are the Laplace transforms of  $\hat{h}(k, t)$  and  $\hat{\psi}(k, t)$ , respectively. After multiplying Eq. (43) by the inverse of matrix  $\mathbb{M}$ , the solutions can be written as

$$\begin{pmatrix} H(k, \omega) \\ \Psi(k, \omega) \end{pmatrix} = \mathbb{M}^{-1} \begin{pmatrix} \hat{h}(k, 0) \\ \hat{\psi}(k, 0) \end{pmatrix} = \frac{1}{(\omega - \omega_1)(\omega - \omega_2)} \begin{pmatrix} \omega - \omega_\psi & -a_h \\ -a_\psi & \omega - \omega_h \end{pmatrix} \begin{pmatrix} \hat{h}(k, 0) \\ \hat{\psi}(k, 0) \end{pmatrix}. \quad (44)$$

The poles of these expressions,  $\omega_1$  and  $\omega_2$ , are the roots of the determinant of  $\mathbb{M}$ . The condition of vanishing determinant yields the dispersion relations for the two normal modes (see Appendix B), which are given by

$$\omega_{1,2} = \omega_s \pm \Omega, \quad (45)$$

where

$$\Omega = \sqrt{a_h a_\psi + \omega_m^2} = \sqrt{(\omega_m - \phi_0 a_h)^2 + \phi_0 B_1 B_3 k^4}, \quad (46)$$

and following definitions were used

$$\omega_s = \frac{1}{2}(\omega_h + \omega_\psi), \quad \text{and} \quad \omega_m = \frac{1}{2}(\omega_h - \omega_\psi). \quad (47)$$

The general solution of the problem is found by performing the inverse Laplace transform of Eq. (44), which leads to

$$\begin{pmatrix} \hat{h}(k, t) \\ \hat{\psi}(k, t) \end{pmatrix} = e^{\omega_s t} \mathbb{A}(k, t) \begin{pmatrix} \hat{h}(k, 0) \\ \hat{\psi}(k, 0) \end{pmatrix}. \quad (48)$$

The form of the matrix  $\mathbb{A}(k, t)$  depends on whether  $\Omega$  is real, imaginary or zero. In the following, we consider each case separately. To simplify the presentation of the results, we will refer to the evolution when  $\Omega$  is imaginary as oscillatory, and to the one when  $\Omega$  is real as monotonic. These regimes are discussed in the Sections 3.1 - 3.3, and summarized in Sec. 3.4. Figure 3 is a diagram that will be useful to determine the different classes of time evolution expected in a system with a certain  $\tau$  and  $\chi$ , when all other parameters are given. The reader may find useful to consult this figure as various stability regimes are discussed. We note that all considered regimes lead to decreasing free energy defined by Eq. (1), as expected.

### 3.1. Imaginary $\Omega$ : Oscillatory evolution

For imaginary  $\Omega$ , it is convenient to write  $\Omega = i\omega_i$ . Using this notation,  $\mathbb{A}$  in Eq. (48) is given by

$$\mathbb{A}(k, t) = \mathbb{I} \cos \omega_i t + \begin{pmatrix} \omega_m & -a_h \\ -a_\psi & -\omega_m \end{pmatrix} \frac{\sin \omega_i t}{\omega_i}. \quad (49)$$

Therefore, the amplitudes of the perturbations oscillate with frequency  $\omega_i$  and they could be damped or growing depending on the sign of  $\omega_s$ .

A necessary condition for having  $\omega$  imaginary is that  $B_1 B_3 < 0$  (see Eq. (46)). Note that this is not sufficient, since there is also a dependence on  $k$ . For  $\tau > 0$ , both  $B_1$  and  $B_3$  are positive (see also Fig. 2 for  $\zeta > 1$ ). When  $\tau < 0$ ,  $B_3$  becomes negative. Then, the necessary condition requires  $B_1 > 0$ , which in turn implies that  $\tau > \tau_1$  with

$$\tau_1 = -\frac{3\nu_0}{2K\delta^2 \left[ \hat{F}'_0 - \left(1 + \frac{\chi}{2}\right) \hat{F}_0 \right]}. \quad (50)$$

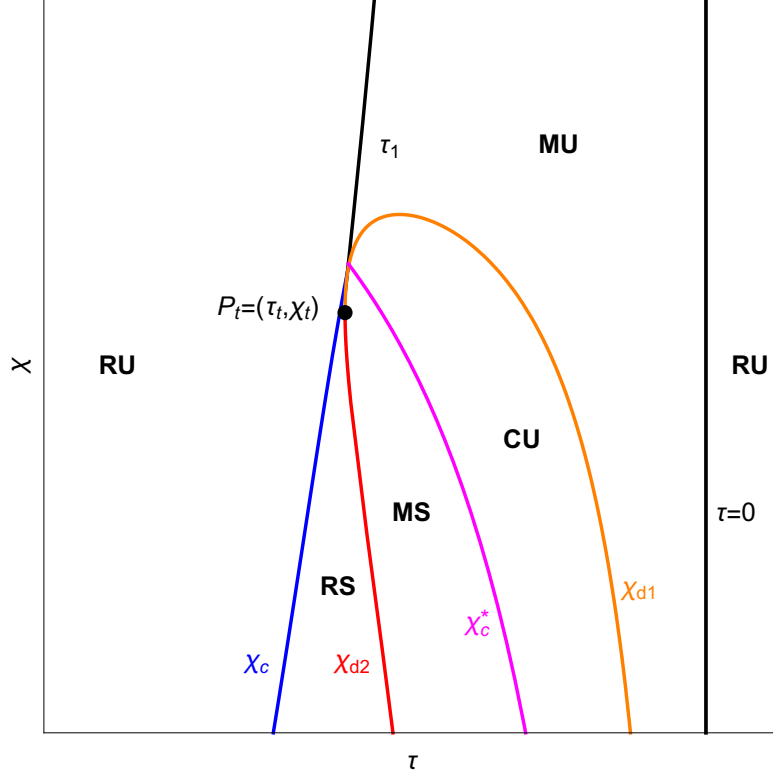


Figure 3: Sketch of the stability diagram as a function of  $\tau$  and  $\chi$ . Note that  $\tau > -1$  and  $0 < \chi < 1$ . The critical lines for the existence of different types of time evolution as described in the text are shown.

It is clear from our argument that no oscillatory evolution is possible if  $\tau > 0$  or  $\tau < \tau_1$  for a given  $\chi$ . The black lines in Fig. 3 show  $\tau = 0$  and  $\tau_1$ . Moreover, since by definition  $\nu_0 > 0$  in Eq. (27), this means that the oscillatory behaviour can only occur if

$$\tau_1 < \tau < 0, \quad (51)$$

but this does not ensure its appearance because additional conditions are required. We note in passing that the zero case ( $\tau = \nu_0 = 0$ ) cannot lead to imaginary  $\Omega$  and therefore the dependence of fluid-solid interaction potential on concentration is necessary to have an oscillatory evolution.

In order to obtain the additional conditions, let us write  $\Omega$  from Eq. (46) in the form

$$\Omega = k^2 \sqrt{(B_2 \phi_0 + \hat{k}_h^2 - \hat{\omega}_\psi^0 \hat{k}_\psi^2 - Ck^2)^2 + 4B_1 B_3 \phi_0}, \quad (52)$$

with

$$C = 1 - \hat{\omega}_\psi^0 - \nu_0 \phi_0 = 1 - 3D\Sigma\phi_0 - \nu_0\phi_0, \quad (53)$$

see Eq. (41). Then,  $\Omega$  vanishes at most at three values of  $k^2$  since

$$\Omega = k^2 \sqrt{C^2(k^2 - k_{d1}^2)(k^2 - k_{d2}^2)}. \quad (54)$$

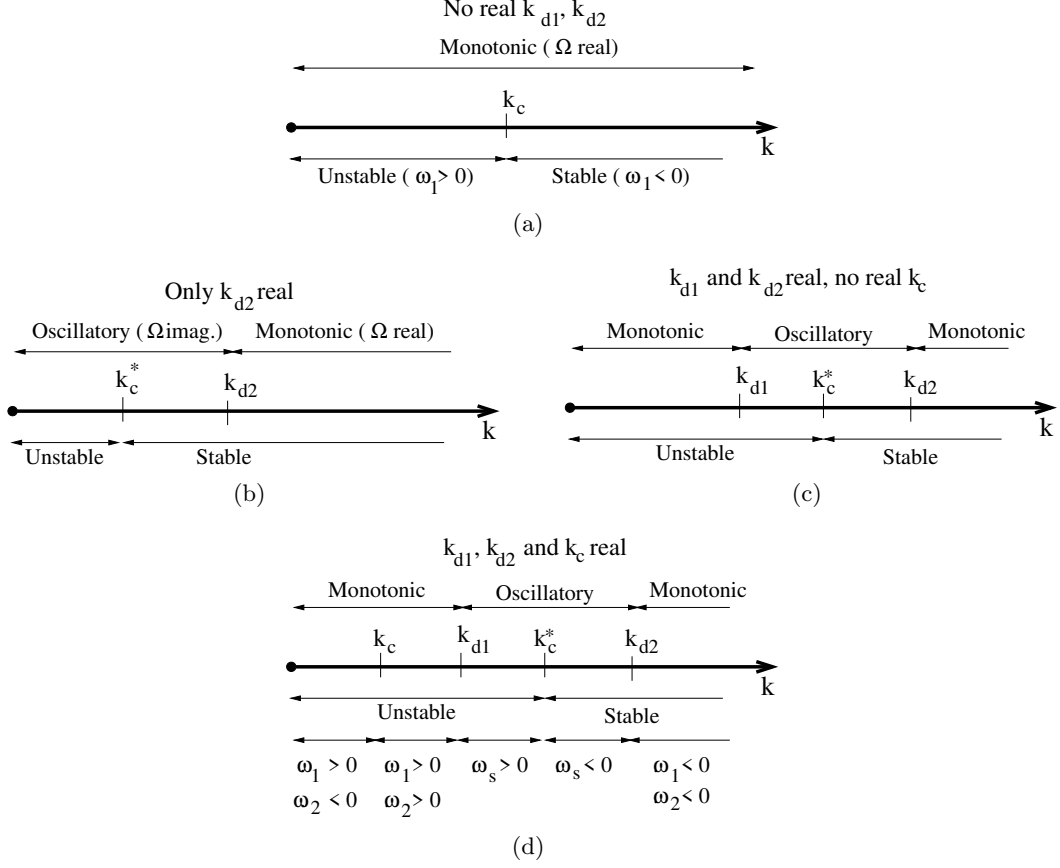


Figure 4: Relative positions of the critical values of  $k$  for: (a) monotonic evolution for all  $k$ , (b) oscillatory evolution for  $0 < k < k_{d2}$ , (c) oscillatory evolution for  $0 < k_{d1} < k < k_{d2}$  and *no real*  $k_c$ , (d) oscillatory evolution for  $0 < k_{d1} < k < k_{d2}$  and *real*  $k_c$ . See the text for definition of various values of  $k$  and  $\omega$ .

In addition to trivial root  $k = 0$ , there are two additional roots  $k_{d1}$  and  $k_{d2}$  given by

$$k_{d1,2}^2 = \frac{1}{C} \left( B_2 \phi_0 + \hat{k}_h^2 - \hat{\omega}_\psi^0 \hat{k}_\psi^2 \mp 2\sqrt{-B_1 B_3 \phi_0} \right). \quad (55)$$

Figure 4 shows the stability as well as the regions in the  $k$ -space where oscillatory behaviour exist. Since the oscillatory behaviour disappears at the points where  $\Omega = 0$ , the sufficient condition for the existence of oscillatory perturbations in a  $k$  interval are  $k_{d1} < k < k_{d2}$ , if  $k_{d1,2}^2 > 0$  (see Figs. 4c and d), or  $0 < k < k_{d2}$ , if  $k_{d1}^2 < 0$  and  $k_{d2}^2 > 0$  (see Figure 4b). Note that if  $k_{d2}^2 < 0$ ,  $\Omega$  is real for all  $k$  (see Fig. 4a).

From Eq. (55) we obtain

$$C^2 k_{d1}^2 k_{d2}^2 \equiv 4B_1 B_3 \phi_0 + \left( B_2 \phi_0 + \hat{k}_h^2 - \hat{\omega}_\psi^0 \hat{k}_\psi^2 \right)^2. \quad (56)$$

The requirement of  $k_{d1}^2 = 0$  or  $k_{d2}^2 = 0$  is equivalent to finding the zeros of the r.h.s.



of Eq. (56), yielding a new condition that involves both  $\tau$  and  $\chi$  (see Eq. (42)). The resulting equation can be solved for  $\chi$  as a function of  $\tau$  to yield two curves in the parameter space, namely  $\chi_{d1}$  and  $\chi_{d2}$ , corresponding to  $k_{d1} = 0$  and  $k_{d2} = 0$ , respectively (orange and red curves in Fig. 3). Then,  $\chi_{d1}$  distinguishes between oscillatory behaviour for  $0 < k_{d1} < k < k_{d2}$  ( $\chi > \chi_{d1}$ ) as in Figs. 4c and d, and those where oscillatory behaviour is present for  $0 < k < k_{d2}$  ( $\chi_{d2} < \chi < \chi_{d1}$ ) as in Fig. 4b. Also,  $\chi_{d2}$  separates regions in the parameter space where oscillatory evolution exist for  $0 < k < k_{d2}$  from those where this type of behaviour is precluded for all  $k$ 's (i.e.  $k_{d1,2}$  imaginary), as in Fig. 4a. Of course, the previous general condition given by Eq. (51) should be satisfied in addition to these new ones to make the oscillatory behaviour possible.

The point  $P_t = (\tau_t, \chi_t)$  in Fig. 3 corresponds to  $\chi_{d1} = \chi_{d2}$ . For  $\tau < \tau_t$ , no  $k$  will lead to an oscillatory behavior since both  $k_{d1}$  and  $k_{d2}$  disappear. Then, the condition  $\tau > \tau_1$  becomes irrelevant for  $\tau < \tau_t$ . As a consequence the line  $\tau_1$  is shown only for  $\tau > \tau_t$  in Fig. 3.

The oscillatory evolution could be either damped or growing, depending on the sign of  $\omega_s$ . Separating these two types of behaviour is the value of  $k = k_c^*$  such that  $\omega_s(k_c^*) = 0$ . From Eq. (47), and using Eq. (38), we can explicitly write  $\omega_s$  as

$$\omega_s(k) = k^2 \left[ \phi_0 B_2 + \hat{k}_h^2 + \hat{\omega}_\psi^0 \hat{k}_\psi^2 - k^2(1 + \hat{\omega}_\psi^0 - \nu_0 \phi_0) \right] = C_1 k^2 (k_c^{*2} - k^2), \quad (57)$$

with

$$C_1 = 1 + \hat{\omega}_\psi^0 - \nu_0 \phi_0, \quad (58)$$

and

$$k_c^* = \sqrt{\frac{\phi_0 B_2 + \hat{k}_h^2 + \hat{\omega}_\psi^0 \hat{k}_\psi^2}{C_1}} = \sqrt{\frac{K \tau \phi_0 \left( \hat{F}_0'' + \frac{3}{2} \chi \hat{F}_0' \right) + K \hat{F}_0'' + 3\beta D \phi_0 G_0''}{\nu_0 \phi_0 - 1 - 3D \Sigma \phi_0}}. \quad (59)$$

Thus, we can conclude that unstable oscillations occur if  $k_{d1} < k < \min(k_c^*, k_{d2})$  (see Fig. 4). In order to ensure that a real  $k_c^*$  exists when  $C_1 \equiv 1 + \hat{\omega}_\psi^0 - \nu_0 \phi_0 > 0$ , it is required that

$$\phi_0 B_2 + \hat{k}_h^2 + \hat{\omega}_\psi^0 \hat{k}_\psi^2 \geq 0.$$

Then, there is a critical condition for the existence of  $k_c^*$  given by

$$\chi \geq \chi_c^* = -2 \frac{K \hat{F}_0'' (1 + \tau \phi_0) + 3\beta D \phi_0 G_0''}{3K \hat{F}_0' \tau \phi_0}. \quad (60)$$

As a corollary, the oscillatory evolution is unstable for  $\chi \geq \chi_c^*$  and  $\tau_1 < \tau < 0$ , but stable otherwise. The critical line  $\chi_c^*$  is shown in Fig. 3 as a magenta curve.

On the other hand, if  $C_1 < 0$ , existence of real  $k_c^*$  requires that  $\phi_0 B_2 + \hat{k}_h^2 + \hat{\omega}_\psi^0 \hat{k}_\psi^2 < 0$ , and the oscillatory evolution is unstable for  $\chi \leq \chi_c^*$  and  $\tau_1 < \tau < 0$ , but stable otherwise. We will see that this case is not possible for reasonable experimental conditions in the context of the application discussed in Sec. 4 (however, it may be relevant to other applications).

### 3.2. $\Omega = 0$ : Critical evolution

Here we discuss the special case that occurs for the wavenumbers  $k_{d1}$  and  $k_{d2}$  (in general,  $k_d$ ) that satisfy

$$\Omega(k_d) = 0.$$

This case corresponds to a situation where the determinant of  $\mathbb{M}$  defined by Eq. (43) has a double root. In this case, the evolution matrix  $\mathbb{A}$  in Eq. (48) takes the form

$$\mathbb{A}(k_d, t) = \mathbb{I} + \begin{pmatrix} \omega_m & -a_h \\ -a_\psi & -\omega_m \end{pmatrix} t. \quad (61)$$

Therefore, the time evolution is not purely exponential, but it contains a term of the form  $te^{\omega_s t}$ . In a formulation of normal modes (see Appendix B) this situation has not a straightforward solution since two exponential normal modes do not exist. Note that  $k = k_d$  is a necessary condition for the transition from monotonic to oscillatory perturbations, but it is not sufficient, since a degeneracy of two monotonic normal modes without the appearance of oscillatory modes is also possible. Such degeneracy occurs when  $k_{d1} = k_{d2}$  for special values of the parameters  $\nu_0$  and  $\tau$ .

### 3.3. $\Omega$ real: Monotonic evolution

For  $\Omega$  real, the matrix  $\mathbb{A}(k, t)$  in Eq. (48) can be written as

$$\mathbb{A}(k, t) = \mathbb{I} \cosh \Omega t + \begin{pmatrix} \omega_m & -a_h \\ -a_\psi & -\omega_m \end{pmatrix} \frac{\sinh \Omega t}{\Omega}. \quad (62)$$

We note that for  $t \rightarrow \infty$ , both  $\sinh \Omega t$  and  $\cosh \Omega t$  tend to  $\frac{1}{2}e^{\Omega t}$ . By combining this exponential with the prefactor  $e^{\omega_s t}$ , we find a single exponential growth rate  $\omega_1 = \omega_s + \Omega$ . Then, the asymptotic behavior of  $\hat{h}$  and  $\hat{\psi}$  is governed by  $\omega_1$ .

In the zero case ( $\nu_0 = \tau = 0$ ), the dispersion relations are given by the expressions for  $\omega_h^0$  and  $\omega_\psi^0$ , see Eqs. (39) and (40). When we include *only* the effects of Marangoni forces ( $\nu_0 \neq 0$ ), while keeping  $\tau = 0$  (the value of  $\chi$  is irrelevant), we have  $B_3 = 0$  and the value of  $\Omega$  is real. Then, from Eq. (46) we have  $\Omega = \omega_m - \phi_0 a_h$  (keeping positive sign without loss of generality), so that now the dispersion relations, Eq. (45), are

$$\omega_1 = \omega_h - \phi_0 a_h = \omega_h^0 + \phi_0 \nu_0 k^4, \quad \omega_2 = \omega_\psi + \phi_0 a_h = \omega_\psi^0.$$

Therefore, we can conclude that the Marangoni effect alone leads to a change in  $\omega_1$  (the asymptotic growth rate) relative to a case when it is ignored ( $\nu_0 = 0$ ), while no change is produced in  $\omega_2$ . However, even in this simple case there is a coupling between  $h$  and  $\psi$ , since the non-diagonal term,  $a_h$  in Eq. (37), is non zero. The same results are obtained also for nonzero  $\tau$  as long as  $\chi = 1$  (that is, including only Hamaker constant dependence on surface concentration,  $\Gamma$ ), since again  $B_1 = 0$ .

When  $\tau \neq 0$  and  $\chi < 1$  ( $B_3 \neq 0$ ),  $\Omega$  will be real, see Eq. (46), if  $B_1 B_3 > 0$ . Then, there is monotonic evolution for  $\tau > 0$  since both  $B_3$  and  $B_1$  are positive. When  $\tau < 0$ ,

the situation is more complicated as the sign of  $B_3$  becomes negative. If  $\tau < \tau_1$ , the condition  $B_1 < 0$  is satisfied, and this ensures a monotonic evolution for all  $k$ 's.

However, if  $\tau > \tau_1$ , it is possible to have monotonic evolution for certain values of  $k$  outside the interval  $(k_{d1}, k_{d2})$ , while oscillatory evolution exists for those  $k$ 's inside the interval (see Fig. 4). If one wants to ensure that the behavior is always monotonic for  $\tau < 0$  and any  $k$ , this interval should disappear. This happens when both  $k_{d1}$  and  $k_{d2}$  are imaginary. Then, the condition  $\chi < \chi_{d2}$  is relevant for  $\tau > \tau_1$  in order to attain monotonic behaviour for all  $k$ 's.

Of course, if  $\chi > \chi_{d2}$  and  $\tau < 0$ , the only possibility for exclusive monotonic evolution is the above mentioned condition  $\tau > \tau_1$  (see Fig. 3). Note that the lines  $\chi_{d1,2}$  and  $\tau_1$  touch each other for a particular value of  $\tau$ . Above this value,  $\chi_{d2}$  is irrelevant.

In the *general case*, the monotonic evolution can be either stable or unstable depending on the signs of  $\omega_1$  and  $\omega_2$ . The critical (marginal) wavenumbers,  $k_c$ , such that either  $\omega_1$  or  $\omega_2$  are zero, satisfy the condition

$$\omega_1\omega_2 = 0 \quad \Rightarrow \quad \omega_s^2(k_c) - \Omega^2(k_c) = 0. \quad (63)$$

This expression is convenient because it avoids the square roots in  $\Omega$  and only requires to find the roots of a polynomial in  $k_c$ . Using Eq. (54) for  $\Omega$  and Eq. (57) for  $\omega_s$ , Eq. (63) (divided by  $k_c^4$  to eliminate the trivial roots  $k_c = 0$ ) can be written as

$$C_1^2(k_c^{*2} - k_c^2)^2 = C^2(k_c^2 - k_{d1}^2)(k_c^2 - k_{d2}^2). \quad (64)$$

This shows that  $k_c$  can only exist outside the interval  $(k_{d1}, k_{d2})$ . Of course, only real and positive  $k_c^2$  roots of this polynomial are physically relevant. Possible situations of this type are shown in Figures 4a and d.

Now, let us consider a case where  $\Omega$  is always real and no oscillatory evolution is possible for any  $k$ . This can happen when both  $k_{d1}^2$  and  $k_{d2}^2$  are negative ( $\chi < \chi_{d1}$  or  $\tau > \tau_1$ ) or when they degenerate to the same value. The critical condition for the existence of only monotonic stable evolution implies that the unstable region  $k \in (0, k_c)$  disappears. This happens when  $k_c = 0$  in Eq. (64), i.e.,  $C_1^2 k_c^{*4} = C^2 k_{d1}^2 k_{d2}^2$ . This condition, by using Eqs. (56) and (59), is equivalent to

$$(1 - \hat{\omega}_\psi^0 - \nu_0 \phi_0) \left( \phi_0 B_2 + \hat{k}_h^2 + \hat{\omega}_\psi^0 \hat{k}_\psi^2 \right)^2 = 4B_1 B_3 \phi_0 + \left( \phi_0 B_2 + \hat{k}_h^2 - \hat{\omega}_\psi^0 \hat{k}_\psi^2 \right)^2. \quad (65)$$

The values of  $\chi$  (as a function of  $\tau$ ) such that this condition is satisfied can be obtained analytically, see Eqs. (38) - (42). The line corresponding to  $\chi_c$  is shown as a blue line in Fig. 3. Then, a monotonic stable evolution is the only possibility, if  $\chi_c < \chi < \chi_{d2}$ .

Finally, we note that behaviour of the perturbations for  $k \rightarrow \infty$  is always stable and real, since to the leading order in  $k$ ,  $\Omega + \omega_s \rightarrow -2\omega\psi^0 k^4$ .

### 3.4. Stability diagrams; Summary

Our formulation allows for a full description of the behavior of a perturbation at any time and not only at its asymptotic limit. However, it is clear from the results that a

real evolution of an arbitrary perturbation is strongly dependent on the parameters of the system, and whether there are  $k$ 's in the decomposition of an initial perturbation that lead to one or another type of evolution. In order to consider these points, we recapitulate our results using the stability diagram given in Fig. 3.

The stability analysis allows to distinguish the following five classes:

1. **Real unstable class (RU)**: There is at least one monotonic unstable perturbation and there are no oscillatory ones ( $\Omega$  is real for all  $k$ ). Since oscillatory behaviour is precluded for all  $k$ 's, this case is possible only for  $\tau < \tau_1$  or  $\tau > 0$ . If a real  $k_d$  exists, it is a double root of  $\Omega$  ( $k_{d1} = k_{d2}$ ). For this class,  $k_c$  is real with unstable evolution if  $k < k_c$ . This class corresponds to the situation depicted in Fig. 4a.
2. **Mixed unstable class (MU)**: Either oscillatory growing perturbations (imaginary  $\Omega$  and  $\omega_s > 0$ ) or monotonically growing perturbations ( $\omega_1$  real and positive) are possible in different  $k$ -ranges. This class requires two distinct positive real  $k_{d1}$  and  $k_{d2}$ , with  $k_{d1} < k_c^* < k_{d2}$ . It corresponds to the situation depicted in Fig. 4c (no real  $k_c$ ) and d (real  $k_c$ ).
3. **Complex unstable class (CU)**: There are oscillatory growing perturbations (imaginary  $\Omega$  and  $\omega_s > 0$  for a certain  $k$ -range) but no monotonic unstable evolution is possible, i.e.,  $\omega_1$  cannot be real and positive for any  $k$ . Note, however, that stable monotonic perturbations are not precluded for some  $k$  values. There is only one positive root at  $k_{d2}$  ( $k_{d1}^2 < 0$ ) and  $0 < k_c^* < k_{d2}$ . The complex unstable behaviour occurs when  $k$  is in the unstable range  $0 < k < k_c^*$ . This class corresponds to the situation depicted in Fig. 4b.
4. **Mixed stable class (MS)**: Only stable perturbations are possible for all  $k$ 's, but they may have either a damped oscillatory behaviour (imaginary  $\Omega$  and  $\omega_s < 0$ ), or their amplitudes may decrease without oscillations, i.e.,  $\omega_1$  is negative. This class appears when there are damped oscillations in the region  $0 < k < k_{d2}$ , while a perturbation is monotonically decreasing otherwise. This corresponds to a case similar to Fig. 4b, but when  $k_c$  does not exist.
5. **Real stable class (RS)**: The perturbations are stable without oscillations, i.e.,  $\Omega$  is real and  $\omega_1$  is negative for all  $k$ 's. This class is possible when  $k_{d2} = 0$ , or no real  $k_d$  exists. All perturbations decrease in magnitude monotonically. Note that the line  $\tau_1$  is not relevant in this region, while  $\chi < \chi_{d2}$  is a required condition for the existence of this class.

The transitions between classes as illustrated in Fig. 3 are the following:

- The transitions **RU–MU** occur at the black lines  $\tau = 0$  and  $\tau = \tau_1$  for  $\tau > \tau_t$ , see point  $P_t$  in Fig. 3.
- The transition **MU–CU** occurs along the orange curve  $\chi_{d1}$  where  $k_{d1} = 0$ .

- The boundary between **CU–MS** is given by the condition that  $\Omega$  is imaginary (oscillatory perturbations are possible in  $0 < k < k_{d1}$ ),  $k_c^* = 0$  (oscillatory growing perturbations are marginal) and  $\omega_s = 0$  (the oscillatory perturbations transition from stable to unstable). The first condition means that the boundary is limited to the region  $\tau_1 < \tau < 0$ , while the remaining ones combined lead to  $\chi = \chi_c^*$  (magenta curve in Fig. 3).
- The boundary **MS–RS** is given by the lowest root of Eq. (56) (red curve  $\chi_{d2}$  in Fig. 3).
- The boundary **RS–RU** is given by  $\chi_c$  (blue line in Fig. 3).

Finally, note that the lines are physically relevant as long as they are present in the region of  $\tau > -1$ .

### 3.5. Expressions for the concentration

Although it is more convenient to consider  $(h, \psi)$ , since these variables are conserved (see Eqs. (28a) and (28b)), the concentration  $\phi_p(x, t)$  is physically relevant since its spatial and temporal variations specify phase separation in the mixture. We begin by noting that to  $O(\epsilon)$ , the bulk concentration,  $\phi$ , is given by

$$\phi(x, t) = \frac{\psi(x, t)}{h(x, t)} \approx \phi_0 + \epsilon \phi_p(x, t),$$

where

$$\phi_p(x, t) = \psi_p(x, t) - \phi_0 h_p(x, t). \quad (66)$$

From Eq. (36), we can write that

$$\hat{\phi}(k, t) = \hat{\psi}(k, t) - \phi_0 \hat{h}(k, t).$$

With the appropriate expression for  $\mathbb{A}(k, t)$ , one can obtain the perturbed concentration  $\hat{\phi}(k, t)$  using Eq. (48).

For the oscillatory evolution case, i.e. for imaginary  $\Omega$ , we use Eq. (49) and the following expression for the concentration ensues

$$\hat{\phi}(k, t) = e^{\omega_s t} \left[ \hat{\phi}(k, 0) \left( \cos \omega_i t + \frac{a_h \phi_0 - \omega_m}{\omega_i} \sin \omega_i t \right) - \hat{h}(k, 0) \frac{B_3 k^2}{\omega_i} \sin \omega_i t \right].$$

The critical case ( $\Omega = 0$ ) leads to the following expression for the perturbed concentration

$$\hat{\phi}(k, t) = e^{\omega_s t} \left[ \hat{\phi}(k, 0) (1 + a_h \phi_0 t - \omega_m t) - \hat{h}(k, 0) B_3 k^2 t \right].$$

Finally, the monotonic evolution case ( $\Omega$  real) requires Eq. (62) and leads to

$$\hat{\phi}(k, t) = e^{\omega_s t} \left[ \hat{\phi}(k, 0) \left( \cosh \Omega t + \frac{a_h \phi_0 - \omega_m}{\Omega} \sinh \Omega t \right) - \hat{h}(k, 0) \frac{B_3 k^2}{\Omega} \sinh \Omega t \right].$$

We note that only when  $B_3 = 0$  (i.e., either  $\chi = 1$  or  $\tau = 0$ )  $\hat{\phi}(k, t)$  depends solely on the *initial* perturbed concentration; otherwise, it depends as well on the initial perturbation of the thickness,  $\hat{h}(k, 0)$ . We will return to these expressions when considering applications to metal alloys.

### 3.6. Evolution of the nodes of a simple perturbation

Our analysis allows to consider arbitrary initial perturbations in physical space,  $h_p(x, 0)$  and  $\psi_p(x, 0)$ . In this section, we discuss general features of the linear evolution of such perturbations, since they will be relevant when considering application to a specific system in Sec. 4.

In general, more than a single  $k$  is needed to reproduce a real physical initial perturbation. In order to obtain the evolution of this perturbation, multiple spatial Fourier components with different  $k$ 's are required. First, one should decompose the initial perturbation in all its Fourier components obtaining  $\hat{h}(k, 0)$  and  $\hat{\psi}(k, 0)$ . Then, Eq. (48) should be used to obtain their independent time evolution. Finally, their superposition must be reverted to the spatial dependence using the Fourier transforms given in Eqs. (36). However, in order to obtain some of the most interesting features, there is no need to consider a very complicated case, since they can be deduced from a very simplified initial condition. Let us consider a perturbation for both  $h_p$  and  $\psi_p$ ,

$$h_p(x, 0) = h_{p0} \cos(kx + \varphi_h), \quad \psi_p(x, 0) = \psi_{p0} \cos(kx + \varphi_\psi), \quad (67)$$

which can have different phases  $\varphi_h$  and  $\varphi_\psi$ , while  $h_{p0}$  and  $\psi_{p0}$  are the amplitudes at  $t = 0$ . These perturbations can be written in the Fourier space, according to Eq. (36), as a combination of two components, namely,  $k$  and  $-k$ , as follows

$$\hat{h}(k, 0) = \frac{h_{p0}}{2} e^{i\varphi_h}, \quad \hat{h}(-k, 0) = \frac{h_{p0}}{2} e^{-i\varphi_h}, \quad (68)$$

$$\hat{\psi}(k, 0) = \frac{\psi_{p0}}{2} e^{i\varphi_\psi}, \quad \hat{\psi}(-k, 0) = \frac{\psi_{p0}}{2} e^{-i\varphi_\psi}. \quad (69)$$

Since all the coefficients involved in both  $\mathbb{A}(k, t)$  and  $\omega_s(k)$  of Eq. (48) depend only on even powers of  $k$ , we have  $\mathbb{A}(k, t) = \mathbb{A}(-k, t)$  and  $\omega_s(k) = \omega_s(-k)$ . Therefore, the solution in space and time can be written explicitly by using Eq. (36) as

$$\begin{pmatrix} h_p(x, t) \\ \psi_p(x, t) \end{pmatrix} = e^{\omega_s t} \mathbb{A}(k, t) \begin{pmatrix} h_p(x, 0) \\ \psi_p(x, 0) \end{pmatrix}. \quad (70)$$

One feature of the time evolution of the perturbations is the fact that their nodes, i.e., the locations where either  $h$  or  $\psi$  vanish, may be either stationary or travel along the  $x$  direction. In fact, by considering both  $h_p(x, t) = 0$  and  $\psi_p(x, t) = 0$  in Eq. (70), we find that the trajectories of the nodes result from solving the equations

$$(\Omega \coth \Omega t + \omega_m) h_{p0} \cos(kx + \varphi_h) = a_h \psi_{p0} \cos(kx + \varphi_\psi), \quad (71)$$

$$(\Omega \coth \Omega t - \omega_m) \psi_{p0} \cos(kx + \varphi_\psi) = a_\psi h_{p0} \cos(kx + \varphi_h), \quad (72)$$

where  $\Omega$  can be either real or imaginary. In general, the solutions of these two equations lead to  $x = x_h(t)$  and  $x = x_\psi(t)$ , which determine the time evolution of the respective node positions. However, if  $h_p(x, 0)$  and  $\psi_p(x, 0)$  are *in phase* ( $\varphi_h = \varphi_\psi$ ), these equations become  $x$ -independent, and they lead instead to the times, say  $t_{0,h}$  and  $t_{0,\psi}$ , when either  $h_p$  or  $\psi_p$  vanish all along the spatial domain.

In what follows, we consider separately few different cases, depending on whether  $\Omega$  is real or imaginary, and whether the perturbations are in phase or not.

- $\Omega$  *real*,  $\varphi_h = \varphi_\psi$ . For this case, Eqs. (71) and (72) lead to single values of  $t_{0,h}$  and  $t_{0,\psi}$ , namely,

$$t_{0,h} = \frac{1}{\Omega} \arg \tanh \left( \frac{a_h \psi_{p0} - \omega_m h_{p0}}{\Omega h_{p0}} \right), \quad t_{0,\psi} = \frac{1}{\Omega} \arg \tanh \left( \frac{a_\psi h_{p0} + \omega_m \psi_{p0}}{\Omega \psi_{p0}} \right).$$

These times characterize the transient stage, i.e., when the evolution is strongly dependant on the initial conditions  $h_p(x, 0)$  and  $\psi_p(x, 0)$ . After this stage (i.e. for  $t \gg t_{0,h}, t_{0,\psi}$ ), the system evolves toward its asymptotic regime. Note that the characteristic times,  $t_{0,h}$  and  $t_{0,\psi}$ , are not the same and that they depend not only on the initial conditions, but also on  $k$ .

- $\Omega$  *real*, *arbitrary*  $\varphi_h, \varphi_\psi$ . Eqs. (71) and (72) describe the motion of the nodes, say  $x_h(t)$  and  $x_\psi(t)$ . We note that these equations also show that the nodes of  $h_p$  and  $\psi_p$  coincide only if  $\tanh \Omega t = 1$ , that is for  $t \rightarrow \infty$ . In particular, Eq. (72) shows that  $x_\psi(t)$  will reach the position of an initial node of  $h_p(x, 0)$  at the time given by  $\Omega \coth \Omega t = \omega_m$  if  $\omega_m > \Omega$ . Note that in the zero case ( $\nu_0 = \tau = 0$ ), we have  $a_h = 0$  and  $\omega_m = \Omega$ , so that the original nodes of  $h_p$  are reached by the nodes of  $\psi_p$  only asymptotically. No similar effect is expected for  $x_h$  since  $\Omega \coth \Omega t + \omega_m$  has no zeros, at least for  $\omega_m > 0$ .
- $\Omega$  *imaginary*,  $\varphi_h = \varphi_\psi$ . The oscillatory nature of the perturbations will lead to a succession of times at which they vanish. As can be easily shown by replacing  $\Omega = i\omega_i$  in Eqs. (71) and (72), now we find

$$t_{0,h} = \frac{1}{\omega_i} \arctan \left( \frac{a_h \psi_{p0} - \omega_m h_{p0}}{\omega_i h_{p0}} \right), \quad t_{0,\psi} = \frac{1}{\omega_i} \arctan \left( \frac{a_\psi h_{p0} + \omega_m \psi_{p0}}{\omega_i \psi_{p0}} \right). \quad (73)$$

Here, the coincidence of  $h_p$  and  $\psi_p$  nodes is impossible since the condition is now  $\tan \omega_i t = i$ , independently of the initial phase difference.

- $\Omega$  *imaginary*, *arbitrary*  $\varphi_h, \varphi_\psi$ . In order to illustrate the complexity of the resulting evolution, let us write the perturbations by using the general solution, Eq. (48), and the particular form of  $\mathbb{A}$ , Eq. (49),

$$\begin{aligned} h_p(x, t) &= \frac{e^{\omega_s t}}{\omega_i} [B h_{p0} \cos(kx + \varphi_h) \sin(\omega_i t + \varphi') - a_h \psi_{p0} \cos(kx + \varphi_\psi) \sin(\omega_i t)] \\ \psi_p(x, t) &= \frac{-e^{\omega_s t}}{\omega_i} [B \psi_{p0} \cos(kx + \varphi_\psi) \sin(\omega_i t - \varphi') + a_\psi h_{p0} \cos(kx + \varphi_h) \sin(\omega_i t)] \end{aligned}$$

where

$$B = \sqrt{\omega_i^2 + \omega_m^2}, \quad \tan \varphi' = \frac{\omega_i}{\omega_m}.$$

Here, we can see that each term within the brackets represents a standing wave whose amplitude may grow or decay depending on the sign of  $\omega_s$ . Since these standing waves are out of phase in both time and space, the resulting perturbation will not be a standing wave. As shown previously, only in the case  $\varphi_\psi = \varphi_h$ , the nodes do not move during the evolution.

A more detailed discussion of the perturbation evolution requires the knowledge of specific values of the parameters. Therefore, we discuss in the following section a particular case, for which relevant parameters are known.

## 4. Application to alloys on nanoscale

In this section we consider our results in the context of alloys of nanometric thickness exposed to laser radiation (Diez *et al.*, 2021). The reported experiments consider an alloy such that the fluids  $A$  and  $B$  correspond to silver,  $Ag$ , and nickel,  $Ni$ , respectively. Thus, for the specific alloy  $Ag_{40}Ni_{60}$ , we have  $\phi_0 = 0.4$  as the initial concentration of the  $A$ -component. This configuration was modelled within the scope of the zero case ( $\nu_0 = \tau = 0$ ). The appropriate choice of material parameters for the problem of alloys (binary fluid) was also discussed in Diez *et al.* (2021); in the present work, we follow the same approach and weight-average the parameters of interest. For example, we consider the viscosity,  $\eta$ , and the diffusivity,  $\mathcal{D}$ , of the alloy to be given by a weighted average viscosity and diffusivity, i.e.,

$$\eta = \eta_A \phi_0 + (1 - \phi_0) \eta_B, \quad \mathcal{D} = \mathcal{D}_A \phi_0 + (1 - \phi_0) \mathcal{D}_B,$$

where  $\eta_{A,B}$  and  $\mathcal{D}_{A,B}$  are the corresponding values for the pure fluids. In Diez *et al.* (2021), we also discuss the approach used to deal with the non-constant temperature of the alloys (due to heating and cooling by laser), and for simplicity and brevity, we will not discuss that aspect of the problem further in the present work.

The resulting values of the parameters are shown in the first two columns of Table 2. The third and fourth columns show the corresponding nondimensional constants. We note that for the considered parameters, the resulting time scale, see Eq. (5), becomes  $t_c = 180.47$  ns, where we have used a spatial scale  $\ell = 100$  nm. In the experiments, the liquid lifetime is similar to the duration of laser pulses applied to melt the alloy, which is  $\sim 20$  ns, and represents a nondimensional time  $t \sim 0.11$ . Thus, for  $O(1)$  times (corresponding to a few laser pulses), the transient evolution of the instability may be relevant.

In order to simplify the discussion of the relevance of Marangoni effects ( $\nu_0 \neq 0$ ) and the dependence of fluid-solid interaction energy on concentration ( $\tau \neq 0$ ), we consider the situation such that the zero case ( $\nu_0 = \tau = 0$ ) is stable. One simple way of ensuring



Parameter	Value	Constant	Value
$\phi_0$	0.4	$(n, m)$	(3, 2)
$T$	2200 K	$\hat{K}$	1.081
$h_0$	15 nm	$K$	48.06
$h_e$	1 nm	$\Sigma$	0.0123
$a$	2 nm	$\beta$	2.58
$\mathcal{H}_{ref}$	$2 \times 10^{-17} J$	$D$	0.0146
$\gamma_{ref}$	$0.981 J/m^2$	$h_*$	0.067
$\sigma$	$1.816 \times 10^{-10} J/m$	$\delta$	0.15
$C_G$	1	$\nu_0$	0.516

Table 2: List of dimensional parameters and nondimensional constants that characterize the experimental situation.

that this is the case is to assume that Gibbs energy,  $G(\phi)$  is given by the ideal isotropic function (although strictly speaking such form is available only for small concentration, see Appendix A for further discussion)

$$G(\phi) = -\phi(\log \phi - 1). \quad (74)$$

This choice leads to  $G_{\phi\phi}^0 = -1/\phi_0$ , so that  $\omega_\psi^0 < 0$  for all  $k$  (see Eq. (40)), and the zero case is stable with respect to  $\psi$  perturbations. Therefore, any instabilities will be due to the dependence of the fluid-solid interaction energy on concentration.

In what follows, we use the temperature value of  $T = 2200 K$ , as in Diez *et al.* (2021), and an initial concentration  $\phi_0 = 0.4$ . For this system,  $\tau_1 < -1$  for all possible  $\chi$ 's and  $\chi_{d2}$  does not exist for  $\tau > -1$ . Therefore, all physically possible negative  $\tau$ 's correspond to the **MU** class, and there is always an oscillatory behavior for appropriate  $k$ 's. In the following, we assume  $\tau = -0.5$  and  $\chi = 0.5$ , respectively, with the value of  $\chi$  chosen so to put equal weight on  $\Gamma$  and  $\phi$ . With the parameters specified, we can now also determine the signs of  $C$  and  $C_1$ , see Sec. 3.1. Figure 5 shows that for temperatures greater than 800 K, reasonable for a melted metal, these quantities are positive irrespective of the value of  $\phi_0$ .

Figure 6 shows the corresponding  $\Omega$  and  $\omega_s$ , as given by Eqs. (45) and (46). The  $k$ -interval where  $\Omega$  is imaginary corresponds to  $(k_{d1}, k_{d2}) = (2.057, 2.969)$ , while  $\omega_s = 0$  occurs at  $k_c^* = 2.554$ . Since we will be focusing on unstable behavior, we select values of  $k$  smaller than  $k_c^*$ . The figure shows that LSA predicts that the evolution for  $k < k_{d1}$  is monotonic, while for  $k_{d1} < k < k_c^*$  it is oscillatory. In what follows, we choose  $k = 1.8$  and  $k = 2.2$  to illustrate both types of behaviour, for perturbations both in phase and out of phase. For an interpretation of these results in terms of normal modes, see Appendix B and Fig. 16.

#### 4.1. Unstable monotonic evolution

Figure 7 shows an example of evolution in the case of in-phase perturbations, for  $k = 1.8$ . This figure shows evolution of the amplitudes  $|h_p(0, t)|$ ,  $|\psi_p(0, t)|$  and  $|\phi_p(0, t)|$  for

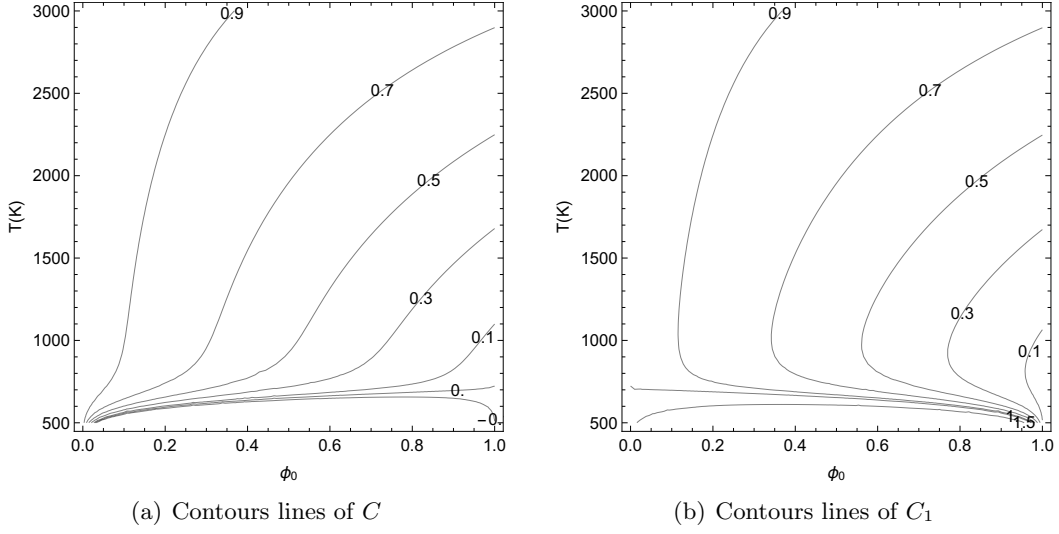


Figure 5: Dependence of  $C$  and  $C_1$  on  $T$  and  $\phi_0$  for the metallic alloy: (a) contour lines of  $C$ , Eq. (53) and (b) idem for  $C_1$ , Eq. (58).

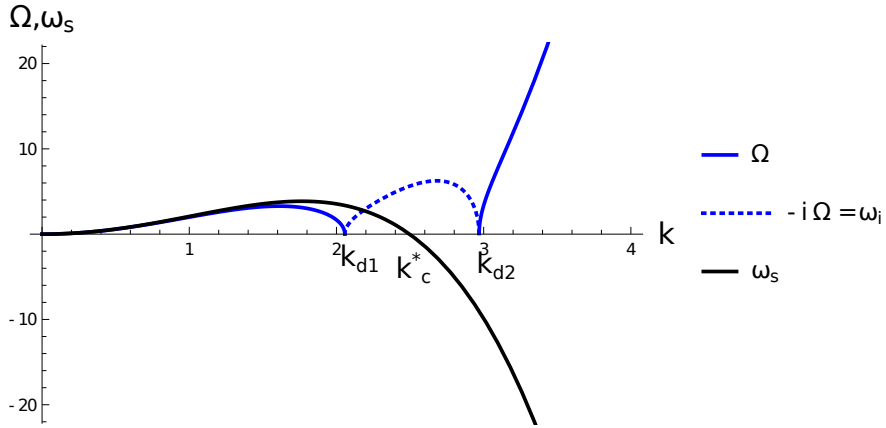


Figure 6: Growth rates  $\Omega$  and  $\omega_s$  from Eqs. (46) and (47), respectively, for the metallic alloy with  $\tau = -0.5$  and  $\chi = 0.5$ . Here,  $(k_{d1}, k_{d2}) = (2.057, 2.969)$  and  $k_c^* = 2.554$ .

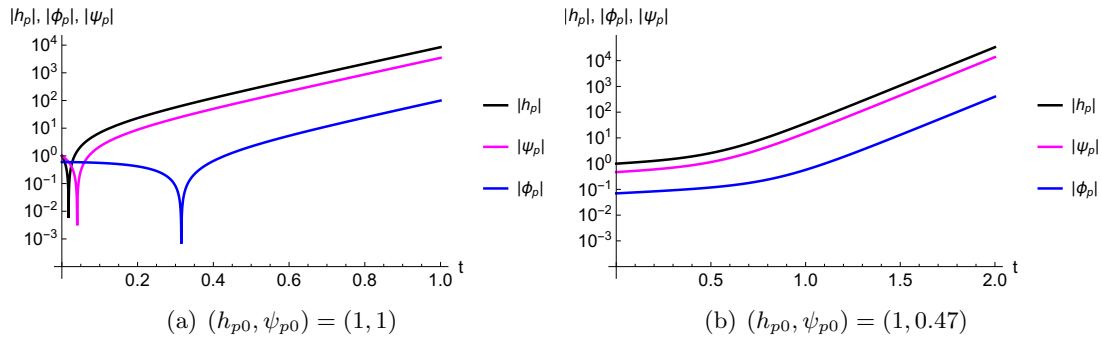


Figure 7: Time evolution of the amplitudes  $|h_p|$  (black),  $|\psi_p|$  (magenta) and  $|\phi_p|$  (blue) for a perturbation of  $k = 1.8$  and in-phase initial conditions,  $(\varphi_h, \varphi_\psi) = (0, 0)$ . Note that the amplitudes shown in part (a) change sign after the dip.

$(h_{p0}, \psi_{p0}) = (1, 1)$  and  $(1, 0.5)$  (see Eqs. (67)–(70) and Eq. (62)). For both cases, the behaviour for large times corresponds to the exponential growth with rate  $\omega_1 = \omega_s + \Omega$ , as expected. However, for early times, the initial conditions may lead to transient evolution which does not correspond to asymptotic behaviour. In fact, for  $(h_{p0}, \psi_{p0}) = (1, 1)$ , we observe that all amplitudes vanish, at the times which are different for each variable, see dips in Fig. 7(a) (note that in the linear approximation,  $\phi_p = \psi_p - \phi_0 h_p$ ). For later times the amplitudes change sign while growing, as expected.

In contrast, for  $(h_{p0}, \psi_{p0}) = (1, 0.47)$  the amplitudes monotonously increase (see Fig. 7(b)). In order to understand the difference between the two cases, we consider Eqs. (71) and (72) for  $\varphi_h = \varphi_\psi = 0$ , and find that

$$\frac{\psi_{p0}}{h_{p0}} = \frac{\Omega \coth \Omega t + \omega_m}{a_h}, \quad \frac{\psi_{p0}}{h_{p0}} = \frac{a_\psi}{\Omega \coth \Omega t - \omega_m}. \quad (75)$$

Note that a solution for finite  $t$  can be found only if

$$\frac{\psi_{p0}}{h_{p0}} > \frac{\Omega + \omega_m}{a_h} = \frac{a_\psi}{\Omega - \omega_m}. \quad (76)$$

In our case, this condition requires  $\psi_{p0}/h_{p0} > 0.4722$ , explaining the differences between cases (a) and (b) in Fig. 7. Therefore, the initial condition can have strong influence on the transient part of the evolution.

Figure 8 illustrates the spatial features of the perturbations for the case  $(h_{p0}, \psi_{p0}) = (1, 1)$ . Note that even if a perturbation can initially be negative at a certain spatial point, it can become positive there for later times, and vice versa.

Let us now consider the influence of a phase difference between the initial perturbations. Our goal is in particular to understand the evolution of perturbations that resemble *Janus-like drops* as illustrated in Fig. 9a.

Figure 10 shows an example where  $\varphi_h = 0$  and  $\varphi_\psi = \pi/3$  with  $(h_{p0}, \psi_{p0}) = (1, 1)$ , leading to  $\varphi_\phi = 0.93 \pi/2$  (see Eqs. (66), (68) and (69)). At  $t = 0$ , the nodes of  $h_{p,n}$  are

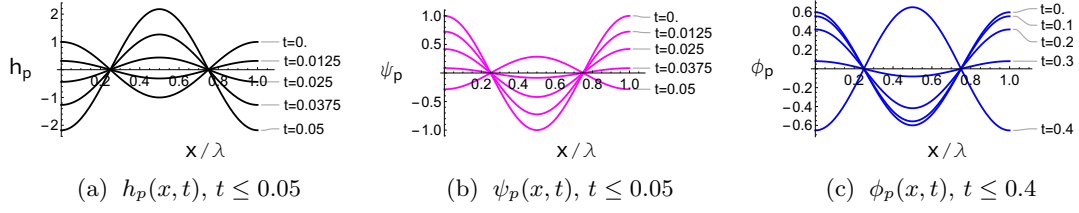


Figure 8: Spatial distribution of the amplitudes  $h_p$  (black),  $\psi_p$  (magenta) and  $\phi_p$  (blue) versus  $x/\lambda$  ( $\lambda = 2\pi/k$ ) for a perturbation of  $k = 1.8$ , in-phase initial conditions with  $(\varphi_h, \varphi_\psi) = (0, 0)$ , and  $(h_{p0}, \psi_{p0}) = (1, 1)$ .

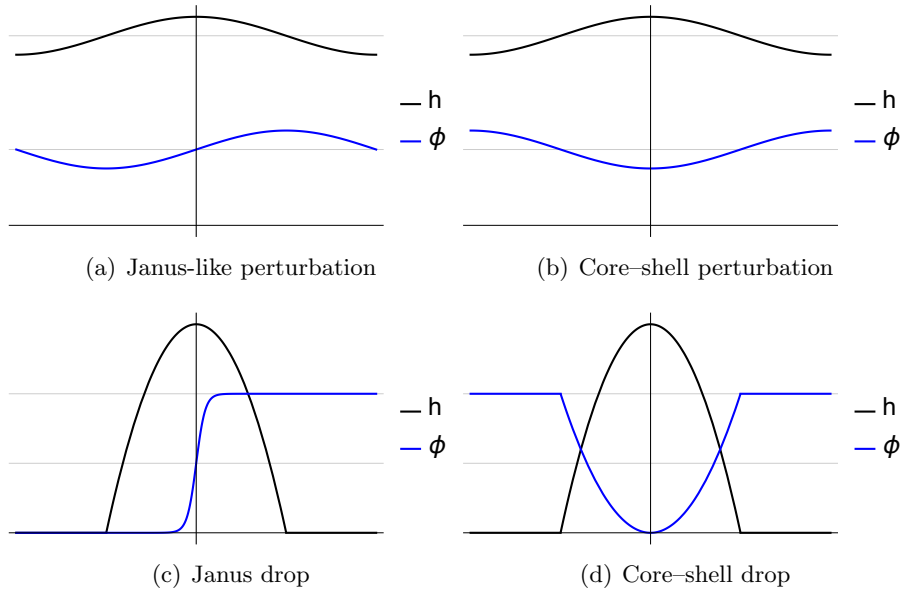


Figure 9: Sketch of the profiles of  $h$  and  $\phi$  for: (a, c) Janus-like perturbation and Janus drop, and (b, d) a core-shell perturbation and core-shell drop.

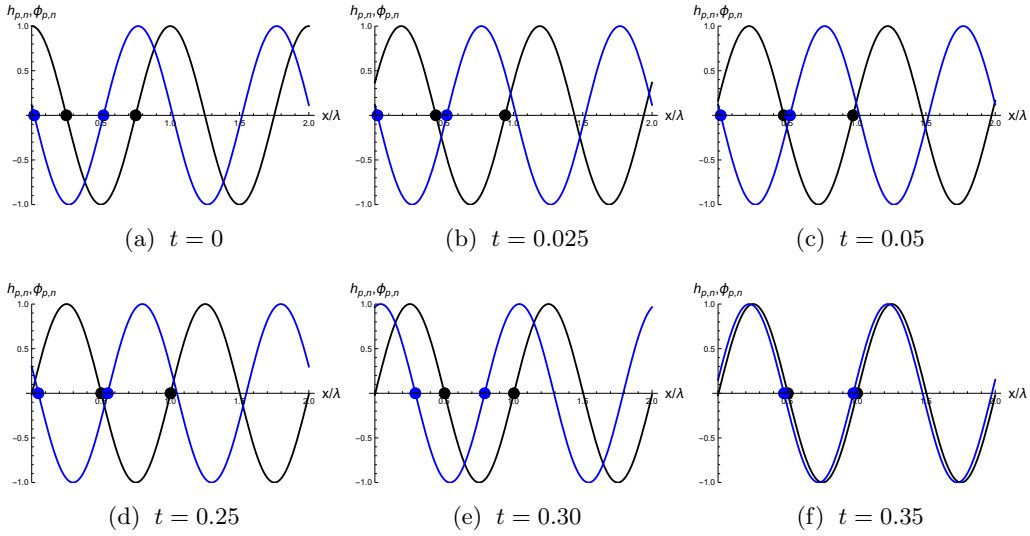


Figure 10: Normalized spatial distribution of the amplitudes values  $h_{p,n} = h_p/h_{p,max}$  (black) and  $\phi_{p,n} = \phi_p/h_{p,max}$  (blue) for a perturbation of  $k = 1.8$  ( $0 < x/\lambda < 2$ ,  $\lambda = 2\pi/k$ ), out-of-phase initial conditions with  $(\varphi_h, \varphi_\psi) = (0, \pi/3)$ , and  $(h_{p0}, \psi_{p0}) = (1, 1)$ . The dots indicate the position of the nodes whose timelines are shown in Fig. 11.

close to the maxima and minima of  $\phi_{p,n}$  and vice versa. In other words, we can think of this initial situation as a Janus-type perturbation. For  $t \approx 0.05$ , these variables reach a counter-phase stage, i.e.,  $\phi_{p,n}$  is minimum where  $h_{p,n}$  is maximum, so that there is a core of  $Ni$  surrounded by a shell of  $Ag$  (with out definition of fluids A and B). However, the configuration keeps on changing for later times, and for times around  $t_{0,\phi} = 0.30$  the system again resembles a Janus structure similar to that at  $t = 0$ . Due to the unstable nature of the perturbation, this second Janus stage corresponds to much larger amplitudes. When this stage is completed, the system rapidly evolves towards a final configuration of the core-shell type (see Fig. 9b), but with a core of  $Ag$  surrounded by a shell of  $Ni$ , since  $h_p$  and  $\phi_p$  are now in phase.

More general manner of tracking the evolution of the perturbations is to consider the nodes of  $h_p$ ,  $\psi_p$  and  $\phi_p$ , which can be calculated from Eqs. (71) and (72). Figure 11 shows the timelines for the interval  $0 < x/\lambda < 1$ . We see that at  $t = 0$  the nodes of both  $h_p$  and  $\phi_p$  are separated a distance  $\approx \lambda/4$  apart. Both  $h_p$  and  $\psi_p$  are practically in phase and remain so for the rest of the evolution. However,  $\phi_p$  reaches a spatial phase difference of  $\lambda/4$  with respect to  $h_p$  for  $t = t_{0,\phi} = 0.297$  (horizontal thin line in Fig. 11). This particular time is given by Eqs. (71) and (72) for both  $x = \lambda/4$  and  $x = 3\lambda/4$ . Therefore, if the amplitudes at this time are sufficiently large and the film breaks up, then Janus drops could be produced. If this is not the case, then only the core-shell type of drops will be obtained, since for later times all three quantities are in phase.

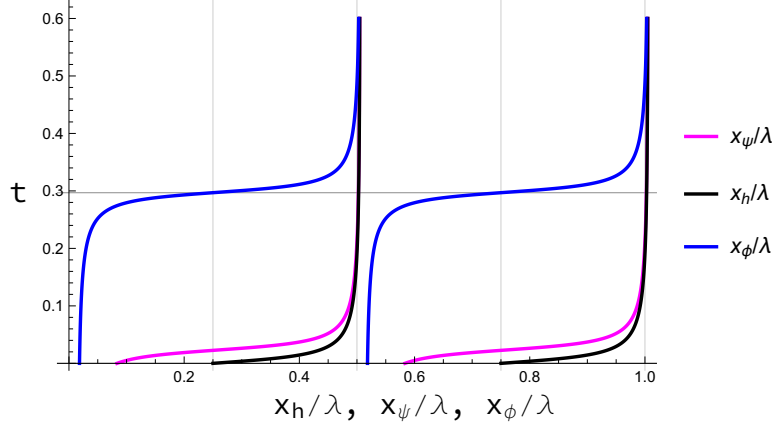


Figure 11: Timelines  $x_h(t)$ ,  $x_\psi(t)$  and  $x_\phi(t)$  of the nodes of  $h_p$  (black),  $\psi_p$  (magenta) and  $\phi_p$  (blue), respectively, for  $k = 1.8$  and  $(\varphi_h, \varphi_\psi) = (0, \pi/3)$  in the interval  $0 < x/\lambda < 1$  with  $\lambda = 2\pi/k$ . The horizontal grid line corresponds to  $t_{0,\phi} = 0.297$ , which is the zero amplitude time for  $\phi_p$  at both  $x = \lambda/4$  and  $3\lambda/4$ .

## 4.2. Unstable oscillatory evolution

In order to analyze an unstable oscillatory case, we choose  $k = 2.2$ , which is in the  $(k_{d1}, k_{d2})$  interval, and start with in-phase perturbations ( $\varphi_h = \varphi_\psi = 0$ ) and initial amplitudes  $(h_{p0}, \psi_{p0}) = (1, 1)$ . The perturbations evolve now in an oscillatory manner with fixed nodes, but the amplitudes of each quantity become zero periodically at times which are independent of the  $x$ -position (i.e., each amplitude passes through zero simultaneously at all points in the domain). In contrast to  $k = 1.8$  case, we have an infinite succession of zero amplitudes times as given by Eq. (73),

$$t_{0,h} = 0.0115 + n\Delta t, \quad t_{0,\psi} = 0.0274 + n\Delta t, \quad t_{0,\phi} = 0.2605 + n\Delta t,$$

where  $\Delta t = \pi/\omega_i = 1.05$ ,  $n = 0, 1, \dots$ , since  $\Omega = i\omega_i$ . Figure 12(a) shows the time evolution of the absolute values of the amplitudes in logarithmic scale so that, similarly to the case shown in Fig. 7(a), the dips indicate the corresponding zero-amplitude times (and consequent change of sign of the amplitude). The growth rates specified by  $\omega_1$  are plotted as dashed lines, showing exponential growth. Figure 12(b) shows the evolution of the amplitudes in a linear plot, where their change of sign is more evident. Unlike the  $k = 1.8$  case, now all initial values  $(h_{p0}, \psi_{p0})$  lead to zeros of the amplitudes for finite times since the hyperbolic cotangent in Eq. (75) turns into a trigonometric one.

Figure 13 shows the spatial dependence of the amplitudes for this oscillatory case. We observe that the nodes are fixed since all perturbations are in phase. Also, we note that the magnitudes vanish at multiple times, in contrast to the  $k = 1.8$  case. Moreover, as a consequence of the oscillatory behaviour at  $k = 2.2$  as well as of the different zero-amplitude times,  $h_p$  and  $\phi_p$  can be of either the same or different sign. For instance, at  $x = 0$  for  $t = 0$  both  $h_p$  and  $\phi_p$  are positive, while we have negative  $h_p$  but positive  $\phi_p$  for  $t = 0.2$ . To be specific, let us identify the maxima of  $h_p$  as the centers of eventual

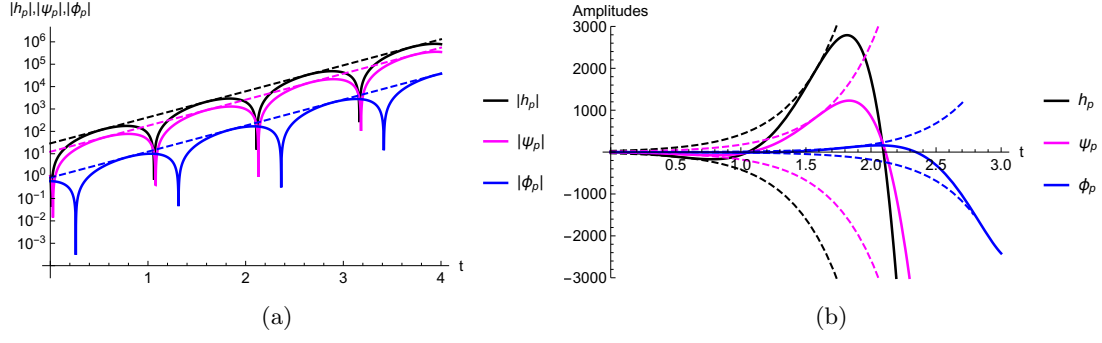


Figure 12: Time evolution of the amplitudes  $h_p$  (black),  $\psi_p$  (magenta) and  $\phi_p$  (blue) at  $x = 0$  for a perturbation of  $k = 2.2$  and in-phase initial conditions,  $(\varphi_h, \varphi_\psi) = (0, 0)$ : (a) Absolute values of the amplitudes in logarithmic scale, (b) Amplitudes in linear scale. The dashed lines are the corresponding exponential envelopes which grow as  $e^{\omega_s t}$ .

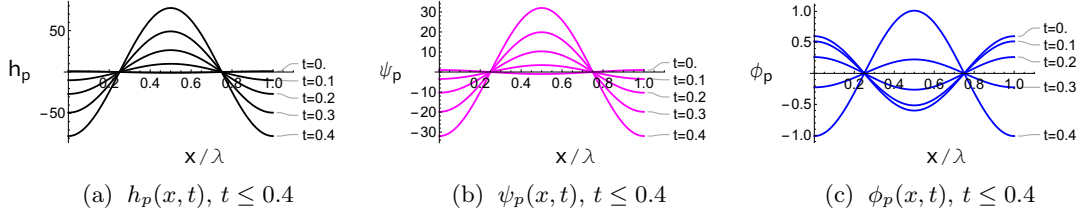


Figure 13: Spatial distribution of the amplitudes  $h_p$  (black),  $\psi_p$  (magenta) and  $\phi_p$  (blue) versus  $x/\lambda$  ( $\lambda = 2\pi/k$ ) for a perturbation of  $k = 2.2$ , in-phase initial conditions with  $(\varphi_h, \varphi_\psi) = (0, 0)$ , and  $(h_{p0}, \psi_{p0}) = (1, 1)$ .

drops and the sign of  $\phi_p$  as the type of dominant metal at that point. Since there is no spatial phase shift, the drops would be of the core-shell type. However, the type of dominant metal in the core changes periodically due to the time delay between  $t_{0,h}$  and  $t_{0,\phi}$ . This is a significant difference compared to the monotonic  $k = 1.8$  case, for which the core structure does not change during the evolution.

When the initial phases differ (e.g.,  $\varphi_h = 0$  and  $\varphi_\psi = \pi/3$ , which implies  $\varphi_\phi = 0.93\pi/2$ ), we can track the nodes (see Fig. 14) as it was done for the  $k = 1.8$  case with the same phase difference. The behaviour at the early stages for  $k = 1.8$  and  $k = 2.2$  is similar (compare Fig. 11 with Fig. 14). However, we have a different value of  $t_{0,\phi}$  for  $x = \lambda/4$ , namely  $t_{0,\phi} = 0.249$ , and also there are repetitive time intervals such that the nodes of  $h_p$  and  $\phi_p$  are  $\lambda/4$  apart, corresponding to  $t_{0,\phi} + n\Delta t$  and  $t_{0,h} + n\Delta t$ , with  $t_{0,h} \approx 0$  and  $\Delta t = 1.05$ , as in the in-phase case for  $k = 2.2$ . Thus, there are successive narrow time-windows where Janus drops could be formed.

Additional insight can be reached by considering the spatial distribution of the amplitudes. Initially, the *drops* are of the Janus-type and rapidly evolve towards a core-shell

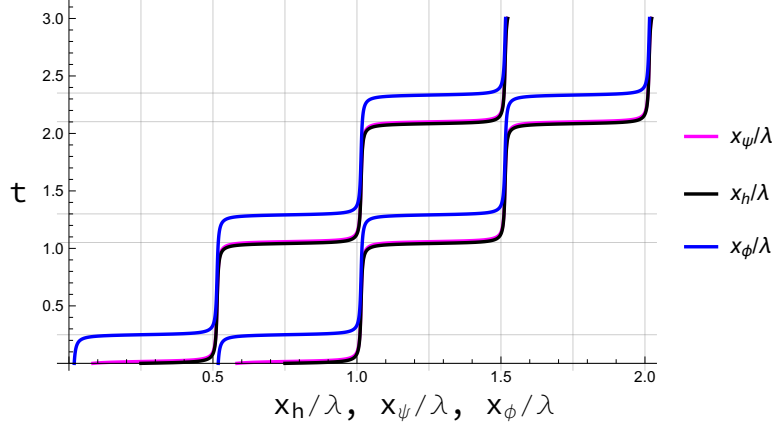


Figure 14: Timelines  $x_h(t)$ ,  $x_\psi(t)$  and  $x_\phi(t)$  in units of  $\lambda = 2\pi/k$  of two consecutive nodes of  $h_p$  (black),  $\psi_p$  (magenta) and  $\phi_p$  (blue), respectively, for  $k = 2.2$  and  $(\varphi_h, \varphi_\psi) = (0, \pi/3)$  in the interval  $0 < x/\lambda < 1$  with  $\lambda = 2\pi/k$ . The horizontal grid lines correspond to  $(t_{0,h} + n\Delta t)$  and  $(t_{0,\phi} + n\Delta t)$  ( $n = 0, 1, \dots$ ), where  $t_{0,h} = 0$  and  $t_{0,\phi} = 0.249$  are the zero amplitude times at both  $x = \lambda/4$  and  $3\lambda/4$ .

type (with a  $N_i$ -core since  $\phi_p$  is minimum where  $h_p$  is maximum) (see top row in Fig. 15). Analogously to the  $k = 1.8$  case with phase shift, the nodes of  $h_p$  and  $\phi_p$  become  $\lambda/4$  apart at  $t_{0,\phi} = 0.249$  (see middle row in Fig. 15). However, the oscillatory nature of the system implies that the behavior repeats itself at times  $\Delta t$  apart. Therefore, the system goes back to recover Janus-type drops, but inverting the position of the metals. Later on, this configuration reaches a core-shell structure, but with an  $Ag$ -core. This process of reversals of both Janus/core-shell drops and materials ( $Ag/Ni$ ) repeats until the final breakup of the film. Therefore, depending on the actual breakup time, one could end up with either Janus-type drops or core-shell ones with cores of either  $Ag$  or  $Ni$ .

## 5. Summary and conclusions

In this paper, we analyze the stability properties of a binary film of nanoscale thickness. Our particular focus is on the development of a model that includes the dependence of the surface tension and of the fluid-solid interaction forces on the concentration field. Due to the complexity of the task on hand, we have implemented various simplifications and have attempted as much as possible to focus only on the main aspects of the problem. Furthermore, to avoid additional difficulties involved in the nonlinear part of the evolution, we focus in the present work only on the linear regime, where at least basic understanding can be reached by linear stability analysis.

While the basic problem (so-called zero-case, where both surface tension and fluid-solid interaction forces are concentration independent) is relatively simple to analyze and understand, the main features of the coupled evolution of film thickness and the



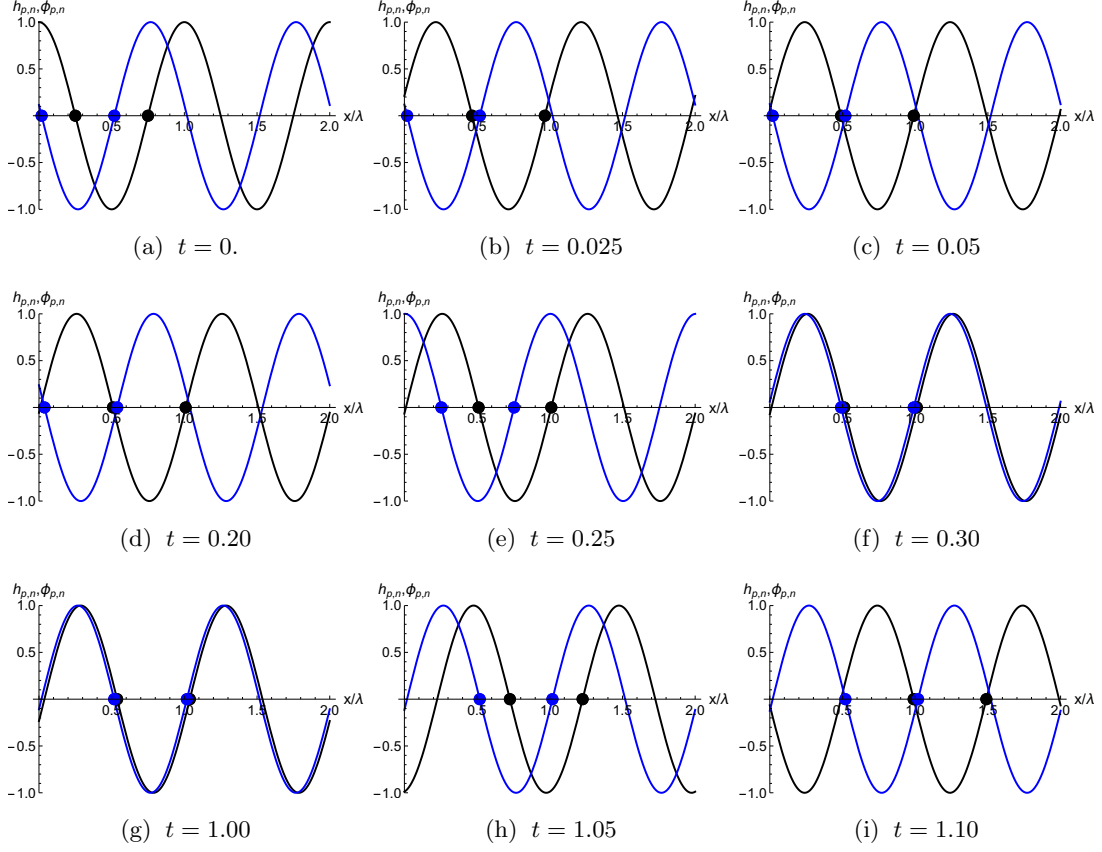


Figure 15: Normalized spatial distribution of the amplitudes  $h_{p,n} = h_p/h_{p,max}$  (black) and  $\phi_{p,n} = \phi_p/h_{p,max}$  (blue) for a perturbation of  $k = 2.2$  ( $0 < x/\lambda < 2$ ,  $\lambda = 2\pi/k$ ), out-of-phase initial conditions with  $(\varphi_h, \varphi_\psi) = (0, \pi/3)$ , and  $(h_{p0}, \psi_{p0}) = (1, 1)$ . The dots indicate the position of the nodes whose timelines are shown in Fig. 14. If the amplitudes are large enough near (e) or (h) to lead to film breakup, then Janus drops will result.

concentration field, for the general case considered in the present paper, evolution of both fields (film thickness,  $h$ , and concentration,  $\phi$ , or consistently,  $h$ , and  $\psi = h\phi$ ) is substantially more involved. In particular, we find that both monotonic and oscillatory evolution is possible, and that various (in)stability regimes exist. The diagram in Fig. 3 illustrates our findings. Depending, in particular, on how fluid–solid interaction forces depend on concentration (in Fig. 3,  $\tau$  is related to the difference of Hamaker constants of the two fluids, and  $\chi$  to the relative importance of surface and volume concentrations), one could find multiple stability regimes corresponding to stable or unstable evolution, as well to oscillatory and monotonic behaviour. Additional complexity comes into play through the dependence of the results on the initial conditions. This result already helps understanding some perhaps unexpected findings in the physical experiments carried out using liquid metals on nanoscale (Diez *et al.*, 2021), where particles of different composition properties are found - both Janus–type of particles, as well as core–shell ones. Our results suggest that both types of particles are possible, with the final outcome depending on the details of inhomogeneities, in addition to material parameters, film thickness, and concentration.

In experiments, often transient stage of instability development is relevant. In the context of metals, this is due to the fact that the metals evolve for a period of time which is determined by the duration of laser pulses used for their melting. This time interval is comparable to the time scale governing the instability development, and therefore the transient features of the instability development are very important. We find that early time transient behaviour may be significantly different compared to the one found for asymptotically long times. For example, we have identified the regimes corresponding to the exchange of concentration (e. g., core shell drops forming, but with periodically changing component which is at the core), among others.

While the considered system definitely leads to a very rich behaviour, our consideration within the asymptotic long wave formulation, combined with a relatively simple model for concentration dependence of fluid–solid interaction and surface tension, has allowed us to formulate a tractable model, such that the main features of the onset of the instability can be understood analytically, at least within the linear regime. The next step in this project should be the implementation of more elaborate analytic methods or accurate simulations which will allow for a better understanding of the nonlinear stages of the instability development. We expect that the results of the present paper will be helpful in carrying out such a task.

**Acknowledgements.** The authors are grateful to R. Allaire, L. Cummings, P. Rack and U. Thiele for many fruitful discussions.

**Funding.** This research was supported by NSF DMS-1815613 (L.K.), NSF CBET-1604351 (L.K., J.A.D., A.G.G.), ACS-PRF 62062-ND9 (L.K.), BSF 2020174 (L.K., J.A.D.) and NJIT faculty seed funding (L.K., J.A.D.). J.A.D and A.G.G. acknowledge support from Consejo Nacional de Investigaciones Científicas y Técnicas (CONICET, Argentina) with Grant PIP 02114-CO/2021 and Agencia Nacional de Promoción Científica

y Tecnológica (ANPCyT, Argentina) with Grant PICT 02119/2020.

## A. Limit of low concentrations

In this limit, the Gibbs energy is given by Eq. (74), so that Eqs. (13) and (18) lead to

$$p_{osm} = \beta\phi, \quad \mu_{osm} = -\beta \log \phi, \quad (77)$$

and assuming that fluid–solid interaction forces do not depend on concentration, we have

$$p_{fs} = K \frac{\partial \hat{F}_{fs}}{\partial h}, \quad \mu_{fs} = 0. \quad (78)$$

Besides, we consider that there are *no interphase interactions*, so that  $\Sigma = 0$ . Therefore, the gradients of total pressure and chemical potentials are (see Eqs. (12), (17) and (15))

$$\nabla p = \nabla (p_{cap} + p_{fs}) + \beta \nabla \phi, \quad \nabla \mu_s = -\frac{\nu}{\delta^2 \phi} \nabla \phi, \quad \nabla \mu = -\frac{\beta}{\phi} \nabla \phi. \quad (79)$$

By replacing these expressions in Eqs. (33a) and (33b), we obtain

$$\frac{\partial h}{\partial t} + \nabla \cdot [-h^3 \nabla (p_{cap} + p_{fs}) + M_a h^2 \nabla \phi] = 0, \quad (80)$$

$$\frac{\partial \psi}{\partial t} + \nabla \cdot [-h^3 \phi \nabla (p_{cap} + p_{fs}) + (M_a h^2 \phi + \tilde{D} h) \nabla \phi] = 0, \quad (81)$$

where

$$M_a = \frac{3\nu}{2\delta^2} = \frac{3k_B T}{2\delta^2 \gamma_{ref} a^2}, \quad \tilde{D} = 3\beta D = \frac{3\mathcal{D}\eta\ell^2}{\gamma_{ref} h_0^3}. \quad (82)$$

Equations (80) and (81) are the nondimensional versions of Eqs. (73) and (74) in Thiele *et al.* (2016). Usually, one finds in the literature that  $p_{cap}$  is given by  $p_{cap} = -\nabla^2 h$ . However, from Eqs. (11) and (13), here we have  $p_{cap} = \nabla \cdot [(1 - \nu\Gamma)\nabla h]$ , so that surface tension dependence on concentration is generally neglected in the capillary pressure (see Thiele *et al.* (2012, 2016); Thiele (2018) for a more extensive discussion on this issue).

## B. Description in terms of normal modes

While we find the Laplace transform method, as discussed in the main body of the paper, appropriate to study both the transitory stage and the asymptotic behaviour, the usual normal mode approach is more common when discussing asymptotic trends. Therefore, we discuss briefly how this alternative approach can be derived from the results developed in the main body of the paper. In order to do so, let us consider the expressions specified by Eq. (44) and write them in the following form

$$\begin{aligned} H(k, \omega) &= \frac{(\omega - \omega_\psi) \hat{h}(k, 0) - a_h \hat{\psi}(k, 0)}{(\omega - \omega_1)(\omega - \omega_2)}, \\ \Psi(k, \omega) &= \frac{(\omega - \omega_h) \hat{\psi}(k, 0) - a_\psi \hat{h}(k, 0)}{(\omega - \omega_1)(\omega - \omega_2)}. \end{aligned} \quad (83)$$

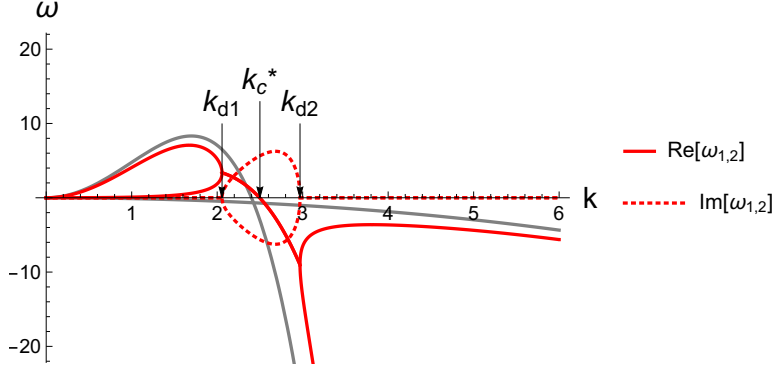


Figure 16: Dispersion relation,  $\omega_{1,2}$ , for the metallic alloy with  $\tau = -0.5$  and  $\chi = 0.5$  (see also Fig. 6). For  $k < k_{d1} = 2.057$  and  $k > k_{d2} = 2.969$ , the upper (lower) solid curves correspond to  $Re[\omega_1]$  ( $Re[\omega_2]$ ), while for  $k_{d1} < k < k_{d2}$  both curves are coincident since here  $Re[\omega_1] = Re[\omega_2]$ . In this interval, both  $Im[\omega_1]$  and  $Im[\omega_2]$  differ only in sign, while  $Im[\omega_1] = Im[\omega_2] = 0$  out of this interval. The critical value  $k_c^* = 2.554$  corresponds to the marginal wavenumber. The grey lines correspond to  $\omega_h^0$  and  $\omega_\psi^0$ , and are shown for comparison.

By expanding these expressions as sums of simple fractions and assuming that  $\omega_1 \neq \omega_2$ , we find

$$\begin{aligned}
 H(k, \omega) &= -\frac{a_h \hat{\psi}(k, 0) + \hat{h}(k, 0)(\omega_\psi - \omega_1)}{(\omega_1 - \omega_2)(\omega - \omega_1)} + \frac{a_h \hat{\psi}(k, 0) + \hat{h}(k, 0)(\omega_\psi - \omega_2)}{(\omega_1 - \omega_2)(\omega - \omega_2)}, \\
 \Psi(k, \omega) &= -\frac{a_\psi \hat{h}(k, 0) + \hat{\psi}(k, 0)(\omega_h - \omega_1)}{(\omega_1 - \omega_2)(\omega - \omega_1)} + \frac{a_\psi \hat{h}(k, 0) + \hat{\psi}(k, 0)(\omega_h - \omega_2)}{(\omega_1 - \omega_2)(\omega - \omega_2)}. \quad (84)
 \end{aligned}$$

The inverse Laplace transforms of these expressions are given by

$$\begin{aligned}
 \hat{h}(k, t) &= -\frac{a_h \hat{\psi}(k, 0) + \hat{h}(k, 0)(\omega_\psi - \omega_1)}{(\omega_1 - \omega_2)} e^{\omega_1 t} + \frac{a_h \hat{\psi}(k, 0) + \hat{h}(k, 0)(\omega_\psi - \omega_2)}{(\omega_1 - \omega_2)} e^{\omega_2 t}, \\
 \hat{\psi}(k, t) &= -\frac{a_\psi \hat{h}(k, 0) + \hat{\psi}(k, 0)(\omega_h - \omega_1)}{(\omega_1 - \omega_2)} e^{\omega_1 t} + \frac{a_\psi \hat{h}(k, 0) + \hat{\psi}(k, 0)(\omega_h - \omega_2)}{(\omega_1 - \omega_2)} e^{\omega_2 t}. \quad (85)
 \end{aligned}$$

These expressions show, as expected, that the solution of the LSA, namely the Fourier transforms  $\hat{h}(k, t)$  and  $\hat{\psi}(k, t)$ , is the superposition of two usual normal modes with eigenvalues  $\omega_1$  and  $\omega_2$  (see Eq. (45)), whenever  $\omega_1$  and  $\omega_2$  are different. Otherwise, the time dependence is not merely exponential as discussed for the critical case in Section 3.2.

Figure 16 shows  $\omega_{1,2}$  for the special case considered in Section 4 for  $\tau = -0.5$  and  $\chi = 0.5$ , where oscillating modes are possible in the interval  $(k_{d1}, k_{d2}) = (2.057, 2.969)$  (see also Fig. 6) in which  $Im(\omega_2) = -Im(\omega_1)$  (dotted lines) and  $Re(\omega_2) = Re(\omega_1)$ .

## References

- BATSON, W., CUMMINGS, L. J., SHIROKOFF, D. & KONDIC, L. 2019 Oscillatory thermocapillary instability of a film heated by a thick substrate. *J. Fluid. Mech.* **872**, 928.
- CAHN, J. W. & HILLIARD, J. E. 1958 Free energy of a nonuniform system. 1. Interfacial free energy. *J. Chem. Phys.* **28**, 258.
- CHAO, RAMÍREZ-SOTO, O., BAHRA, C. & KARPITSCHKA, S. 2022 How liquid–liquid phase separation induces active spreading. *Proced. Nat. Acad. Sciencis (PNAS)* **119**, 2203510119.
- CLARKE, N. 2005 Toward a model for pattern formation in ultrathin-film binary mixtures. *Macromolecules* **38**, 6775–6778.
- CRASTER, R.V. & MATAR, O.K. 2009 Dynamics and stability of thin liquid films. *Rev. Mod. Phys.* **81**, 1131.
- DIAMANT, H. & ANDELMAN, D. 1996 Kinetics of surfactant adsorption at fluid–fluid interfaces. *J. Phys. Chem.* **100**, 13732.
- DIEZ, J. A., GONZÁLEZ, A. G., GARFINKEL, D. A., RACK, P. D., MCKEOWN, J. T. & KONDIC, L. 2021 Simultaneous decomposition and dewetting of nanoscale alloys: A comparison of experiment and theory. *Langmuir* **37**, 2575–2585.
- DOI, M. 2011 Onsager’s variational principle in soft matter. *J. Phys.: Condens. Matter* **23**, 284118.
- DONG, N. & KONDIC, L. 2016 Instability of nanometric fluid films on a thermally conductive substrate. *Phys. Rev. Fluids* **1**, 063901.
- GIRIFALCO, L. A. & GOOD, R. J. 1957 A theory for the estimation of surface and interfacial energies i: Derivation and application to interfacial tension. *J. J. Phys. Chem.* **61**, 904–909.
- HUGHES, R. A., MENUMEROV, E. & NERETINA, S. 2017 When lithography meets self-assembly: a review of recent advances in the directed assembly of complex metal nanostructures on planar and textured surfaces. *Nanotechnology* **28**, 282002.
- ISRAELACHVILI, JACOB N. 1992 *Intermolecular and surface forces*. New York: Academic Press, second edition.
- JOSEPH, D. D., BAI, R., CHEN, K. P. & RENARDY, Y. Y. 1997 Core-annular flows. *Annu. Rev. Fluid. Mech.* **29**, 65.
- JOSEPH, D. D. & RENARDY, Y. Y. 1992a *Fundamentals of Two-Fluid Dynamics. Volume 1: Mathematical Theory and Applications*. Springer-Verlag.

- JOSEPH, D. D. & RENARDY, Y. Y. 1992*b* *Fundamentals of Two-Fluid Dynamics. Volume 2: Lubricated Transport, Drops and Miscible Fluids*. Springer-Verlag.
- KARPITSCHKA, S. & RIEGLER, H. 2012 Noncoalescence of sessile drops from different but miscible liquids: Hydrodynamic analysis of the twin drop contour as a self-stabilizing traveling wave. *Phys. Rev. Lett.* **109**, 066103–5.
- KARPITSCHKA, S. & RIEGLER, H. 2014 Sharp transition between coalescence and non-coalescence of sessile drops. *J. Fluid Mech.* **743**, R1.
- KHENNER, M. 2018 Modeling solid-state dewetting of a single-crystal binary alloy thin films. *J. Appl. Physics* **123**, 034302.
- KHENNER, M. & HENNER, V. 2020 Modeling evolution of composition patterns in a binary surface alloy. *Modelling Simul. Mater. Sci. Eng.* **29**, 015002.
- KONDIC, L., GONZALEZ, A. G., DIEZ, J. A., FOWLKES, J. D. & RACK, P. 2020 Liquid-state dewetting of pulsed-laser-heated nanoscale metal films and other geometries. *Annu. Rev. Fluid Mech.* **52**, 235.
- MAKAROV, S. V., MILICHKO, V. A., MUKHIN, I. S., SHISHKIN, I. I., ZUEV, D. A., MOZHAROV, A. M., KRASNOK, A. E. & BELOV, P. A. 2016 Controllable femtosecond laser-induced dewetting for plasmonic applications. *Laser Photonics Rev.* **10**, 91.
- MAO, S., KULDINOW, D., HAATAJA, M. P. & KOSMRLJ 2019 Phase behavior and morphology of multicomponent liquid mixtures. *Soft Matter* **15**, 1297–1311.
- MCKEOWN, J. T., WU, Y., FOWLKES, J. D., RACK, P. D. & CAMPBELL, G. H. 2015 Simultaneous in-situ synthesis and characterization of Co@Cu core-shell nanoparticle arrays. *Adv. Mater.* **27**, 1060.
- NÁRAIGH, L. O. & THIFFEAULT, J-L. 2007 Dynamical effects and phase separation in cooled binary fluid films. *Phys. Rev. E* **76**, 035303.
- NÁRAIGH, L. O. & THIFFEAULT, J-L. 2010 Nonlinear dynamics of phase separation in thin films. *Nonlinearity* **23**, 1559–1583.
- ORON, A., DAVIS, S. H. & BANKOFF, S. G. 1997 Long-scale evolution of thin liquid films. *Rev. Mod. Phys.* **69**, 931.
- SHKLYAEV, S., ALABUZHEV, A. A. & KHENNER, M. 2012 Long-wave Marangoni convection in a thin film heated from below. *Phys. Rev. E* **85**, 016328.
- SHKLYAEV, S., NEPOMNYASHCHY, A. A. & ORON, A. 2014 Oscillatory longwave Marangoni convection in a binary liquid. part 2: Square patterns. *SIAM J. Appl. Math.* **74** (4), 1005–1024.
- SPRENGER, W., WALHEIM, S., BUDKOWSKI, A. & STEINER, U. 2003 Toward a model for pattern formation in ultrathin-film binary mixtures. *Interface Science* **11**, 225–235.

- THIELE, U. 2011 Note on thin film equations for solutions and suspensions. *Eur. Phys. J. Special Topics* **197**, 213–220.
- THIELE, U. 2018 Recent advances in and future challenges for mesoscopic hydrodynamic modelling of complex wetting. *Colloids and Surfaces A* **553**, 487–495.
- THIELE, U., ARCHER, A. J. & PISMEN, L. M. 2016 Gradient dynamics models for liquid films with soluble surfactant. *Phys. Rev. Fluids* **1**, 083903.
- THIELE, U., ARCHER, A. J. & PLAPP, M. 2012 Thermodynamically consistent description of the hydrodynamics of free surfaces covered by insoluble surfactants of high concentration. *Phys. Fluids* **24**, 102107.
- THIELE, U., TODOROVA, D. V. & LOPEZ, H. 2013 Gradient dynamics description for films of mixtures and suspensions: Dewetting triggered by coupled film height and concentration fluctuations. *Phys. Rev. Lett.* **111**, 117801.
- THIELE, U., VELARDE, M. G. & NEUFFER, K. 2001 Dewetting: Film rupture by nucleation in the spinodal regime. *Phys. Rev. Lett.* **87**, 016104.
- THOMPSON, C. V. 2012 Solid-state dewetting of thin films. *Annu. Rev. Mater. Res.* **42(1)**, 399–434.
- TODOROVA, D. V. 2013 Modelling of dynamical effects related to the wettability and capillarity of simple and complex liquids. PhD thesis, Loughborough University.
- XU, X., THIELE, U. & QIAN, T. 2015 A variational approach to thin film hydrodynamics of binary mixtures. *J. Phys.: Condens. Matter* **27**, 085005.